Chapter 5
Laser Examples and Their Applications

In this chapter we will investigate different types of practical lasers that are often used in the laboratory. Owing to the recent advances in high-power and high-brightness laser diodes, diode-pumped solid-state lasers are the most important lasers today and into the future. Therefore, the lasers described below all belong to the solid-state laser category, with the exception of the HeNe laser, a gas laser, which is a well known device still widely used as precision alignment laser in the laboratory. Another important gas laser is the CO_2 laser, which uses a molecular transition excited via electronically excited N_2 molecules, using a He buffer gas for cooling and reduction of the lifetime of the lower laser level. This laser is the most efficient gas laser with electrical-to-optical efficiencies of up to 30 %.

Other laser types are, e.g. dye lasers, in which a dye solution is used as the active medium. These lasers were often used to provide wide-band tunable sources from the ultra-violet to the infrared spectral region or to generate ultra-short pulses, as the missing long-range order in the liquid laser medium results in broad transitions.

Also lasers without an active medium exist, the free-electron lasers. In these devices, a relativistic electron beam is sent into an alternating-pole spatially-periodic magnetic field, which forces the electrons on to an undulating path. As these electrons are accelerated charges, they emit a synchrotron radiation with a wavelength that depends on the period of the magnets, the relativistic contraction of this period in the frame of the electron beam and the relativistic Doppler shift back to the laboratory frame.

5.1 Gas Lasers: The Helium-Neon-Laser

The HeNe laser was the first cw laser and also the first gas laser realized. While at that time the strongest transition at 1.15 μm was used, the HeNe lasers today are mainly operated on the visible lines, with the mostly used line at 632.8 nm in the red spectrum. Other important lines are the green 543.3 nm, the yellow 594.1 nm and the orange 611.8 nm lines. Other infrared lines are the near-infrared lines at 1152.3 nm and 1523.1 nm as well as the 3391.3 nm mid-infrared line.

M. Eichhorn, *Laser Physics*, Graduate Texts in Physics,
DOI 10.1007/978-3-319-05128-4_5,

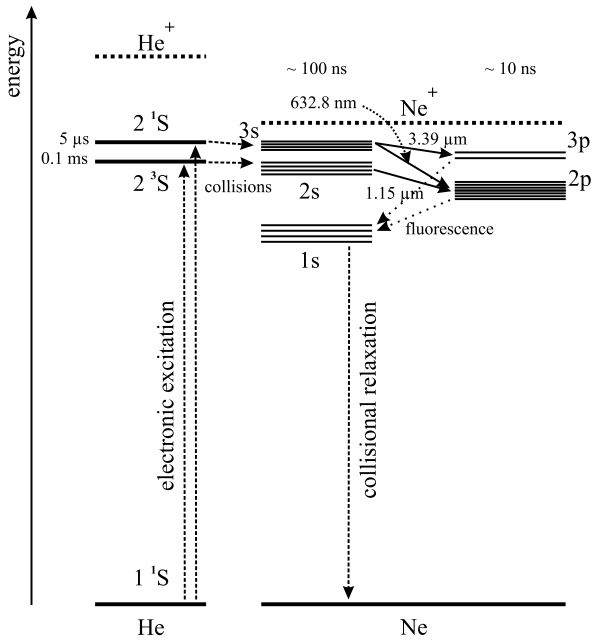

Fig. 5.1 Energy scheme of the HeNe laser including the main transitions

In the HeNe laser [1] the laser active medium is the neon gas. The addition of helium is only used for the pumping process. It also contributes to the cooling of the gas mixture due to the high thermal conductivity of He. Usually, a mixture of about 0.1 mbar Ne in 1 mbar He is used. As can be seen in Fig. 5.1, the pumping of the Ne atoms occurs in an electric discharge in a two-stage process: excitation of He and energy transfer to Ne. First the He atoms are excited by collisions with the electrons in the discharge, bringing them into the metastable levels $2\,^3S$ and $2\,^1S$, with lifetimes of 0.1 ms and 5 µs, respectively. Then, owing to the nearly coincidence between these levels and the $2s$ and $3s$ levels of Ne, the stored energy will be transferred to the Ne atoms in atomic collisions between He and Ne. As the lifetime of the $2s$ and $3s$ levels of Ne is on the order of 100 ns, a population inversion results with respect to the $2p$ and $3p$ levels, which exhibit a lifetime of only around 10 ns. As a result of the selection rules of electric dipole transitions the Ne atoms can only emit on lines connecting a s and a p state, resulting in the above-mentioned laser transitions. From the p states the Ne ions quickly relax to the $1s$ state by fluorescence emission. As this state is also metastable, i.e. long lived, the Ne ions would be re-excited into the $2p$ state by electron collisions, where they would cause a re-absorption on the laser lines terminating in this state. To avoid a strong population of this $1s$ state, small bore discharge tubes are used to cause a decay of this state back to the ground state by collisions with the wall of the laser tube.

Resulting from the dependence of the emission cross-section

$$\sigma_e(\nu_s) \propto \frac{g(\nu_s)}{\nu_s^2} \tag{5.1}$$

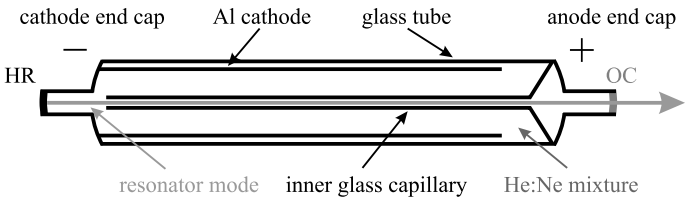

Fig. 5.2 Cut through a typical HeNe laser tube. Here, the resonator mirrors are bonded to the glass tube directly in "hardseal" technology

on the laser frequency ν_s, as shown in Eq. (1.74), and the dependence of the dominating Doppler broadening line form factor from Eq. (1.84), given by

$$g(\nu_s) \propto \frac{1}{\nu_s}, \tag{5.2}$$

the maximum gain of the HeNe laser will be proportional to λ_s^3 and will thus occur on the mid-infrared transition at 3391.3 nm. Therefore, this line will usually show the lowest pump threshold and the HeNe laser would only emit at this line. In order to avoid this effect and to operate the laser on the other lines, special cavity mirrors are used that do not reflect the mid-infrared radiation, thus greatly increasing the threshold power at this line well above the thresholds of the visible lines. A second possibility is to insert a quartz-glass plate, preferentially at Brewster's angle, into the cavity. This strongly increases the intra-cavity losses on the mid-infrared line owing to the internal infrared absorption of the glass whilst nearly no losses are added for the visible-to-near-infrared transitions. Additionally, the laser output will be linearly polarized, as only the s-polarization of the cavity mode will be transmitted through the Brewster plate without Fresnel reflection loss.

The experimental construction scheme of a HeNe laser is shown in Fig. 5.2. The geometry of the capillary has to be chosen in a way so that the product of total gas pressure p and capillary bore diameter d is about $pd \simeq 4.8$–5.3 mm mbar, whilst the optimum mixture between He and Ne depends on the emission line. For the 632.8 nm line, a partial pressure ratio of He : Ne = 5 : 1 is used, whereas an optimum ratio of He : Ne = 9 : 1 was found for the 1152.3 nm line. A third parameter is the discharge current density, which is especially important for the 632.8 nm and 3391.3 nm lines.

The main applications of HeNe lasers today are as alignment sources with high beam quality, caused by the low beam distortions generated in a gas laser, and as highly coherent laser sources in holography, interferometry and ring-laser gyroscopes. As a result of the fact that the laser transitions occur between very high-energetic levels, as can be seen in Fig. 5.1, the quantum efficiency of the HeNe laser is around 10 %. However, the total electrical-to-optical efficiency of the HeNe laser is very low, usually around 0.1 %, which is caused by the low efficiency excitation mechanism within the plasma discharge [1].

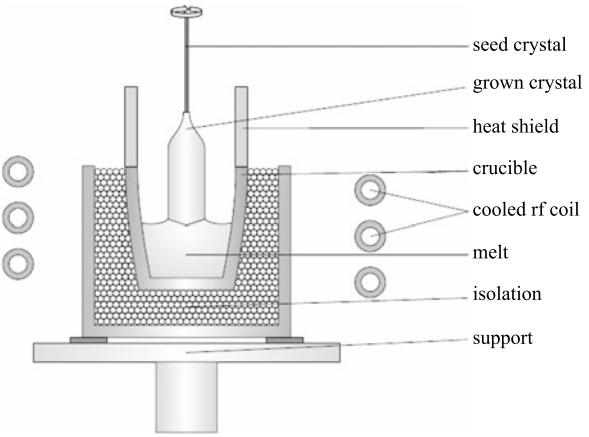

Fig. 5.3 Schematic setup of a Czochralski growth apparatus [12]

5.2 Solid-State Lasers

The most important lasers today are solid-state lasers, in which ionic impurities doped into transparent crystals or glasses act as the laser active species. In general, two main types of hosts and two main types of active ions can be distinguished: crystals and glasses on the one side, and rare-earth ions and transition-metal ions on the other side.

In rare-earth ions, the laser active electronic states are located in the inner $4f$ shell of the ion. Therefore, they are shielded to a great extent from the crystal field by the outer shell electrons ($5s^2$ and $5p^6$ electrons). Thus, the crystal field and the coupling of the ionic states to the phonons of the host lattice is low, resulting in usually narrow line widths for the optical transitions. In the spectra of the rare-earth ions in crystalline media, the different lines of the transitions between the various Stark levels are clearly visible as already shown in Fig. 2.6.

If these rare-earth ions are doped into a glass matrix, the arguments concerning the influence of the crystal field on to the transitions is still valid. However, the glass is an amorphous solid and the geometric structure of the glass matrix, and thus the crystal field varies locally, causing a spatially dependent line shift. This causes an inhomogeneous broadening of the emission spectrum and results in a very broad gain of these laser media. This is important to make broadly tuneable lasers, as well as for the generation of ultra-short pulses.

In contrast to the rare-earth ions, the optically active electrons in transition-metal ions are located in the outer shells of the ion and are thus fully affected by the crystal field. They, therefore, show a very strong coupling to the lattice phonons in crystals, which result in mixed electronic-vibronic states. Owing to this effect the widths of the transition lines are also extremely broad, making e.g. the Ti:sapphire laser so important for the generation of ultra-short pulses.

Crystal Growth Most of the laser crystals used today are grown by the Czochralski method shown in Fig. 5.3. This technique uses a single-crystalline seed, which

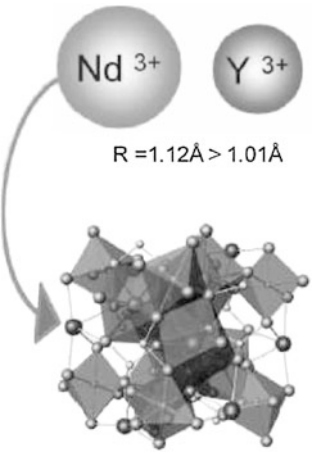

Fig. 5.4 Atomic structure of the YAG crystal and the sites of the Nd^{3+} ion in YAG [13]

is used to pull a large single crystal from a melt, consisting of a stoichiometric composition of primary chemicals. In the case of the well-known laser host yttrium-aluminum-garnet (YAG, $Y_3Al_5O_{12}$), this is a mixture of yttrium oxide and aluminum oxide, to which a small amount of rare-earth oxide, e.g. neodymium oxide, is added, determining the rare-earth dopant concentration of the final laser crystal. The composition is melted in a crucible consisting of a metal of high melting point, such as iridium, which is heated by induction from an external, water-cooled rf coil. The crucible itself is embedded with thermally insulating pellets, such as zirconia. A single crystalline seed is mounted on a rotating rod and brought into contact with the melt. Then, this rotating rod is slowly pulled with a speed of some mm per hour, causing the single crystal to grow. When the growth process is completed, the finished crystal is slowly cooled down to room temperature to anneal internal stress that may have built up during growth.

5.2.1 The Nd^{3+}-Laser

The neodymium laser is one of the mostly used lasers today, operating often on a true four-level transition with an emission wavelength of 1064 nm for Nd^{3+} in YAG as the host crystal. This special host crystal is shown in Fig. 5.4. Where, the Nd^{3+} ion replaces the Y^{3+} ion. However, owing to the larger ionic radius of Nd^{3+} compared with Y^{3+}, only a small fraction of the Nd^{3+} ions are incorporated into the crystal structure during growth, resulting in Nd^{3+} dopant concentrations of usually 0.1–1.2 %, as well as a doping gradient along the growth direction. This gradient is caused by the increased concentration of the Nd^{3+} ions in the melt during growth, resulting in an increase in Nd^{3+} dopant concentration in the crystal towards the end of the growth process.

The energy level scheme of Nd^{3+} ions in different hosts is shown in Fig. 5.5. The upper laser level lifetime in YAG is 250 µs. It is the 1064 nm transition, which

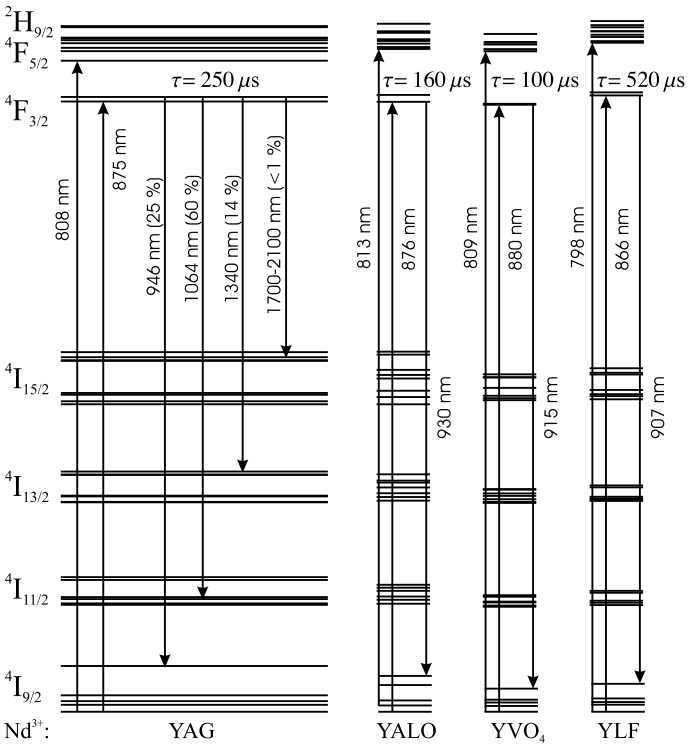

Fig. 5.5 Energy scheme of the Nd^{3+} ion in various hosts and the main pump and laser transitions

shows the largest fluorescence, to which 60 % of all radiatively decaying ions in the $^4F_{3/2}$ manifold contribute to. The fluorescence corresponding to the quasi-three-level transition around 900–950 nm is caused by 25 % of the decaying ions and the second four-level transition at around 1.34 μm arises from a contribution of 14 % of the total decay. The mid-infrared transitions around 2 μm are so weak that they are not used for any practical laser. Owing to the relatively large emission cross section of the 1064 nm transition compared with the 946 nm and the 1342 nm transition, special care has to be taken whenever these two weaker transitions are to be used. In this case, special cavity mirrors and laser media, which are anti-reflection coated at 1064 nm have to be used in order to suppress any feedback on the 1064 nm line. Otherwise, the laser would oscillate on this 1064 nm line, making emission on the other lines impossible by fixing the upper level population to a value that does not allow the threshold gain for the other transitions to be achieved.

The Nd^{3+} ion is either pumped by flashlamps or more recently by high-power laser diodes, which can be directly designed to match the absorption spectrum of the two most important pump transitions at around 808 nm and 875 nm. As a result of this absorption-matched pumping laser-diode-pumped Nd^{3+} lasers show high efficiencies $\gg$40 %, whilst only a small part of the full emission spectrum of a flashlamp will be absorbed by the Nd^{3+} ion, resulting in a total efficiency of usu-

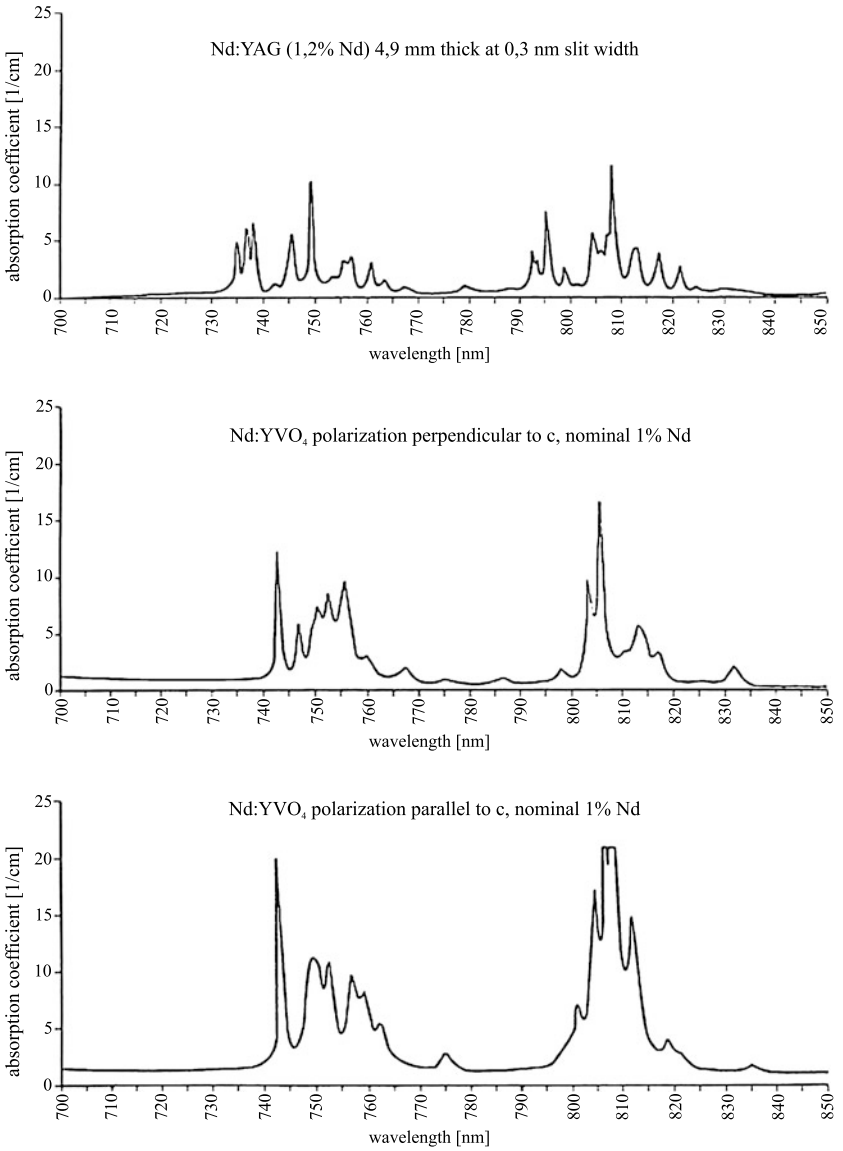

Fig. 5.6 Pump absorption coefficients for Nd^{3+} in different hosts. (Source: Northrop Grumman Corporation, USA)

ally <1 % in flashlamp-pumped lasers. Therefore, flashlamp-pumped Nd^{3+} laser crystals are often co-doped with Cr^{3+} ions, which show a large absorption for the flashlamp emission spectrum. The energy absorbed by the Cr^{3+} ions is then transferred to the Nd^{3+} ions in a direct ion-ion energy transfer process. Diode pumping at around 808 nm on the absorption lines shown in Fig. 5.6 is very popular and led to

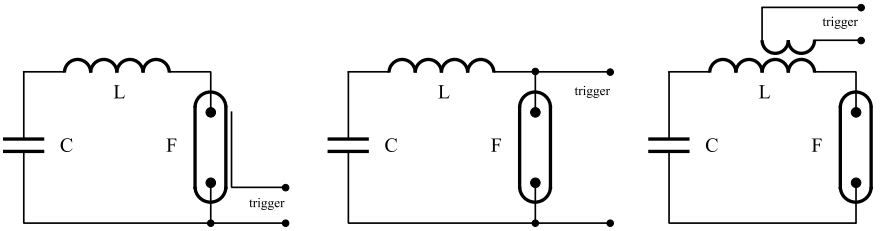

Fig. 5.7 Schematic of simple externally-triggered flashlamp circuits

a large production of laser diodes at this wavelength, which are therefore, relatively cheap. Today laser diodes with high diode output powers are available, generating up to 100 W out of a 200 µm pump delivery fiber.

Flashlamp-Pumped Nd^{3+} Lasers

In a flashlamp-pumped laser, a bank of capacitors is discharged into a flashlamp to produce a high-energy pump pulse for the laser medium. In order to obtain a specific pump pulse duration and pulse form, the electrical characteristics of a flashlamp and the discharge circuit have to be taken into account. Usually, as shown in Fig. 5.7, a charged capacitor C is connected to a flashlamp F via a series inductance L, which determines the discharge time constant

$$T = \sqrt{LC}. \tag{5.3}$$

The charging voltage is, however, too low to "ignite" the flashlamp itself in most cases. Therefore, an external trigger wire is attached to the outside of the flashlamp and a high voltage ignition pulse is applied to this wire to cause a slight ionization of the gas contained in the flashlamp. Then, a small discharge channel is created between the flashlamp electrodes and the main discharge will develop within some 10 µs by increasing the ionization and the diameter of the discharge, until it fills the whole flashlamp tube. For short trigger pulses, the inductor L shows a high dynamic resistance. Thus, the trigger pulse may also directly be connected to the high-voltage side of the flashlamp after the inductor. The inductor then shields the capacitor from the short high-voltage-trigger pulse and the fast rise in voltage across the flashlamp causes breakdown of the gas in the flashlamp. A third possible trigger circuit uses the inductor itself as a secondary of a transformer, and the trigger pulse is applied to the primary. Thus, the trigger pulse will induce a high voltage in the secondary, which adds to the voltage of the capacitor and causes breakdown of the flashlamp.

After the discharge has fully developed and fills the whole flashlamp tube, the flashlamp shows a non-linear resistance and the voltage across the flashlamp U is connected to its current I by [3]

$$U = K_0\sqrt{I}, \tag{5.4}$$

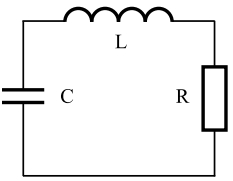

Fig. 5.8 Schematic of a standard RLC circuit

where, K_0 is a parameter of the flashlamp, which is given by the manufacturer or can be measured experimentally. It depends on the geometry of the flashlamp, i.e. its arc length l and the inner tube diameter d, and the gas parameters as

$$K_0 = k\frac{l}{d}. \tag{5.5}$$

For 450 torr xenon-filled flashlamps, a value of $k = 1.27\ \Omega\sqrt{\text{A}}$ is found. Including the dependence on the gas pressure, the flashlamp constant can be described by

$$K_0(P) = K_0(P_0)\left(\frac{P}{P_0}\right)^{\frac{1}{5}} \tag{5.6}$$

for xenon-filled flashlamps. The reference pressure in this case is $P_0 = 450$ torr. For krypton, approximately the same flashlamp constant is found [3]. Thus, the electric resistance of the flashlamp can be described by

$$R_F = \frac{K_0}{\sqrt{I}} \tag{5.7}$$

when the discharge has fully developed.

Another important parameter of a flashlamp is its explosion energy, which gives the amount of electrical input energy that will cause catastrophic damage to the tube wall. This damage is caused by the high temperature of the plasma and especially the acoustic shock wave generated by the plasma, which itself heats up during the pulse from 300 K to about 12000 K. The explosion energy is related to the surface of the inner tube wall ld and the duration of the pulse t_p by

$$E_X = k_X ld\sqrt{t_p}, \tag{5.8}$$

where, k_X is a parameter that depends on the gas filling and gas pressure. Using the definition of the explosion energy the lamp life, i.e. the number of shots N a flashlamp can usually be used at an electrical pulse energy per shot of E_0, can be derived empirically and is related to its single-shot explosion energy by

$$N \approx \left(\frac{E_X}{E_0}\right)^{8.5}. \tag{5.9}$$

Therefore, the lamps usually are operated well below their explosion energy, resulting in a nominal lifetime of 10^6–10^8 shots.

In the case of a constant load resistance R instead of a flashlamp, a standard RLC circuit results as shown in Fig. 5.8. The differential equation governing the discharge evolution of the capacitor in this case is given by

$$L\frac{\partial^2 Q}{\partial t^2} + R\frac{\partial Q}{\partial t} + \frac{Q}{C} = 0, \tag{5.10}$$

where, Q is the charge of the capacitor C and the initial condition is $Q(0) = CU_0$ with $\frac{\partial Q}{\partial t}(0) = 0$. The solution of this equation can be easily found, resulting in a voltage $U(t)$ across the resistor R of

$$U(t) = U_0\frac{\gamma}{\omega}e^{-\gamma t}\left(e^{i\omega t} - e^{-i\omega t}\right), \tag{5.11}$$

with

$$\gamma = \frac{R}{2L} \tag{5.12}$$

$$\omega = \sqrt{\frac{1}{LC} - \gamma^2}. \tag{5.13}$$

The circuit thus shows three different cases of discharge behaviour, depending on the actual values of the components:

- **Underdamped discharge**. Here

$$R < 2\sqrt{\frac{L}{C}}, \tag{5.14}$$

  resulting in a real value of ω. Thus, the current will show an oscillatory behaviour, which is exponentially damped due to the energy dissipation in the resistance R.
- **Overdamped discharge**. Here

$$R > 2\sqrt{\frac{L}{C}}, \tag{5.15}$$

  resulting in an imaginary value of ω. Therefore, no oscillatory current will build up. The high resistance results in a low peak current and it will take a long time until the capacitor is fully discharged. Both of these operation regimes are usually not desired in flashlamp circuits for lasers. The oscillatory discharge causes an erosion of the flashlamp electrodes, which are designed for a specific polarity, and the overdamped discharge results in low pump peak intensities.
- **Critically damped discharge**. In this special case

$$R = 2\sqrt{\frac{L}{C}}, \tag{5.16}$$

  i.e. $\omega = 0$, the current will not show an oscillatory behaviour and the stored energy is delivered to the load in the shortest possible time without oscillation. The absolute values of the current and the voltage follow the relation [3]

$$I(t) = I_{peak}\frac{t}{T}e^{-\frac{t}{T}+1}, \tag{5.17}$$

$$U(t) = 2U_0\frac{t}{T}e^{-\frac{t}{T}}, \tag{5.18}$$

  with $I_{peak} = \frac{2U_0}{eR}$ being the peak discharge current and $T = \sqrt{LC}$ being the time constant of the LC circuit. The current pulse form and the corresponding capacitor voltage is shown in Fig. 5.9.

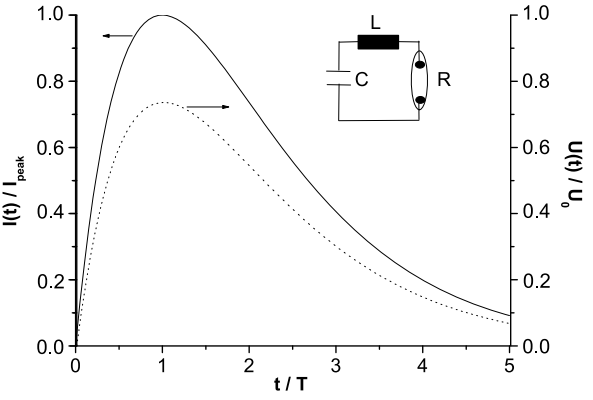

Fig. 5.9 Characteristic current and voltage evolution of a critically-damped discharge circuit

However, in a flashlamp circuit the flashlamp shows a non-linear, current-dependent resistance [3]. Using the definition of the wave resistance

$$Z_0 = \sqrt{\frac{L}{C}}, \tag{5.19}$$

the damping factor γ for the flashlamp is given by

$$\gamma = \frac{K_0}{T\sqrt{U_0 Z_0}}, \tag{5.20}$$

and thus, depends on the starting voltage of the capacitor. The critically damped case usually employed in a laser system corresponds to $\gamma = 0.8T^{-1}$, for which a pulse width of $t_p = 3T$ can be deduced, defined as the time between the 10 % points of the current pulse, and corresponding to approximately 97 % of the total discharge energy delivered to the flashlamp. Using the relation of the stored energy E_0 in the capacitor,

$$E_0 = \frac{1}{2} C U_0^2, \tag{5.21}$$

the necessary capacity is found from (5.20) as

$$C^3 = \frac{2\gamma^4 T^4}{9} \frac{E_0 t_p^2}{K_0^4}, \tag{5.22}$$

resulting for $\gamma = 0.8T^{-1}$ in

$$C^3 = 0.091 \frac{E_0 t_p^2}{K_0^4}. \tag{5.23}$$

Hence, the necessary inductance is

$$L = \frac{t_p^2}{9C}. \tag{5.24}$$

It has to be noted that this calculation gives the design for a critically-damped circuit at a certain lamp energy E_0, and therefore, for a certain capacitor voltage U_0. When

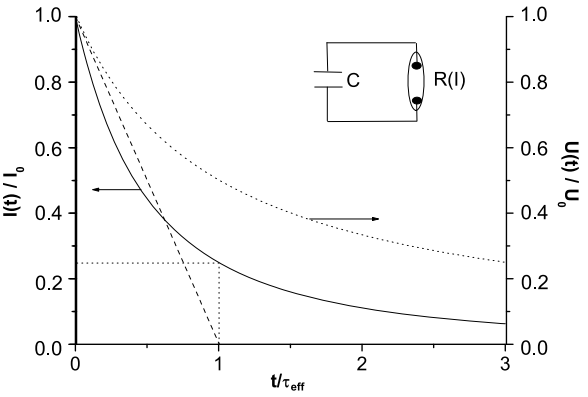

Fig. 5.10 Characteristic current and voltage evolution of an inductance-free discharge circuit

the capacitor is charged to a higher voltage, the system is no longer critically damped and discharge oscillations will occur. For this critically-damped case, it has been found empirically [3] that the explosion energy of a xenon-filled flashlamp can be described by,

$$E_X = 1.2 \times 10^4 \,\mathrm{J\,cm^{-2}\,s^{-1/2}} ld\sqrt{t_p}, \tag{5.25}$$

i.e. a parameter $k_X = 1.2 \times 10^4 \,\mathrm{J\,cm^{-2}\,s^{-1/2}}$.

In some cases, especially for extremely compact lasers and circuits where inductors are not used, then this circuit corresponds to the completely overdamped case. Then, by taking the non-linear resistance of the flashlamp into account, Eq. (5.10) becomes

$$K_0\sqrt{-\frac{\partial Q}{\partial t}} + \frac{Q}{C} = 0, \tag{5.26}$$

where, the current was taken as $I = -\frac{\partial Q}{\partial t}$. We define the effective time constant of the discharge by

$$\tau_{eff} = \frac{K_0^2 C}{U_0}, \tag{5.27}$$

which depends on the charging voltage U_0 of the capacitor. Then, we obtain for the capacitor voltage $U(t)$ and the circuit current $I(t)$

$$U(t) = \frac{U_0}{\frac{t}{\tau_{eff}} + 1}, \tag{5.28}$$

$$I(t) = \frac{I_0}{(\frac{t}{\tau_{eff}} + 1)^2}, \tag{5.29}$$

with a peak current of

$$I_0 = \frac{U_0^2}{K_0^2}. \tag{5.30}$$

The characteristic pulse form is shown in Fig. 5.10. The energy delivered to the flashlamp during the time τ_{eff} is given by

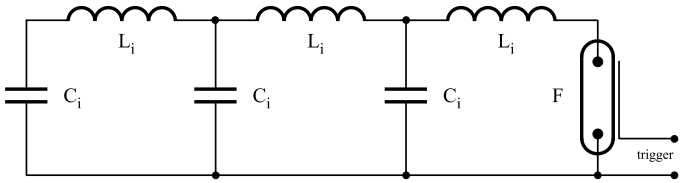

Fig. 5.11 Schematic of a transmission-line flashlamp circuit for rectangular pulses

$$E(\tau_{eff}) = \int_0^{\tau_{eff}} U(t)I(t)dt = \frac{3}{4}E_0. \tag{5.31}$$

After a time of $2\tau_{eff}$, ~89 % of the total energy has been delivered to the flashlamp.

Often, a more rectangular pulse shape is required, especially in free-running lasers, which should emit a rectangular laser pulse. In this case, the total capacity C_{tot} and the total inductance L_{tot} have to be devided as shown in Fig. 5.11, to form a transmission line [3]. Each mesh of this transmission line consists of an LC circuit with $L_i = \frac{L_{tot}}{n}$ and $C_i = \frac{C_{tot}}{n}$, with n being the number of meshes within the transmission line. The characteristic impedance of the transmission line,

$$Z = \sqrt{\frac{L_{tot}}{C_{tot}}}, \tag{5.32}$$

is then chosen to match the load resistance of the flashlamp $R(I) = Z$ at the requisite current. It is convenient to define the pulse width t_p^* in this case, as the time between the 70 % points of the current pulse, resulting in

$$t_p^* = 2\sqrt{L_{tot}C_{tot}} = 2T, \tag{5.33}$$

from which the necessary total capacity

$$C_{tot} = \frac{t_p^*}{2Z} \tag{5.34}$$

and the inductance

$$L_{tot} = \frac{t_p^* Z}{2} \tag{5.35}$$

can directly be calculated. The peak current of the discharge is then given by

$$I_{peak} = \frac{U_0}{2Z}. \tag{5.36}$$

Thus, the charging voltage of the transmission line needs to be set in order to achieve the impedance matching between the transmission line and the current-dependent resistance of the flashlamp. The rise time of the pulse measured between the 10 % and the 80 % point decreases with the number of meshes n as

$$t_r^* = \frac{t_p^*}{2n}. \tag{5.37}$$

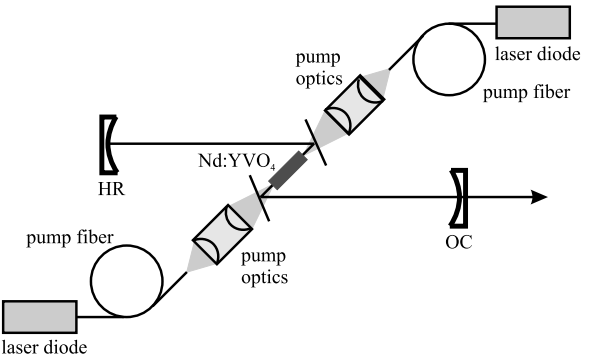

Fig. 5.12 Schematic setup of a fiber-coupled laser-diode-pumped Nd^{3+}:YVO_4 laser [3]

A high number of meshes results in a more and more rectangular pulse. The necessary total capacity can be derived from (5.21), (5.33) and (5.36) and results in

$$C_{tot}^3 = \frac{1}{8}\frac{E_0 t_p^{*2}}{K_0^4}. \tag{5.38}$$

Laser-Diode-Pumped Nd^{3+} Lasers

A Nd^{3+} laser, pumped by fiber-coupled laser diodes, is shown in Fig. 5.12 as an example of a longitudinally pumped Nd^{3+}:YVO_4 medium. The cavity is folded by the use of two dichroic mirrors, which are highly reflecting under the chosen angle of incidence for the laser radiation, whilst being highly transmissive for the diode pump beam. The pump output of the delivery fiber is first collimated by a lens and then focused into the crystal with an appropriate focal length in order to get a pump spot that is well matched to the fundamental mode distribution of the cavity inside the laser crystal. The fibers used for high-power pumping are usually multi-mode fibers. Thus, the pump beam propagation can be described by standard geometrical optics. The two main important parameters of the fiber, are its core diameter d and its numerical aperture NA, which is determined by the refractive-index difference in a step-index fiber as

$$\mathrm{NA} = \sqrt{n_{core}^2 - n_{cladding}^2}. \tag{5.39}$$

The numerical aperture also describes the half-angle θ_f of the radiation emitted by the fiber, given by

$$\mathrm{NA} = \sin\theta_f. \tag{5.40}$$

Usually, the pump optics consist of a two-lens telescope, where, the first lens collimates the beam emitted by the fiber, and the second lens refocuses the beam to form the pump spot in the crystal. When we denote the magnification

$$M = \frac{2r_p}{d} \tag{5.41}$$

of the telescope as the ratio between pump-spot diameter to fiber core diameter, the internal angle of the pump radiation in the crystal can be described by

$$\theta_i = \arcsin\left(\frac{1}{n}\sin\left[\frac{\arcsin \mathrm{NA}}{M}\right]\right) \approx \frac{\mathrm{NA}}{nM}, \tag{5.42}$$

which can be approximated in most cases for small values of the NA, where, n is the refractive index of the laser crystal. Thus, especially when long laser media are used, the pump beam inside the crystal is no longer a cylindric volume. To describe the laser behaviour in this case, especially the threshold pump power, we have to define an effective pump beam radius $w_{p,eff}$ and thus, an effective pump beam area A_{eff}. To model the laser output power, the already known linear relation with respect to pump power given by

$$P_{out} = \eta_{slope}(P_p - P_{th}) \tag{5.43}$$

is used, with the threshold pump power

$$P_{th} = \frac{I_{sat}^{p} A_{eff}}{\eta_{abs}}\left(\ln G + \sigma_a(\lambda_s)\langle N\rangle L\right) \tag{5.44}$$

and the slope efficiency

$$\eta_{slope} = \eta_{mode}\frac{\lambda_p}{\lambda_s}\frac{-\ln(1-T_{OC})}{2\ln G}\eta_{abs}, \tag{5.45}$$

where, $T_{OC} = 1 - R_{OC}$ is the output coupler transmission,

$$\eta_{abs} = 1 - e^{-\alpha_p L} \tag{5.46}$$

the fraction of absorbed pump power, α_p the pump absorption coefficient, $\langle N\rangle$ the average dopant ion density, I_{sat}^{p} the pump saturation intensity, G the single-pass gain, and $A = \pi w_{eff}^2$ the effective pump beam area. As pump and laser beam often do not overlap exactly, a mode fill efficiency η_{mode} is introduced into the slope efficiency. To find a description for the effective pump beam radius, we have to take into account the fact that the beam radius will change axially as a result of focusing and that the pump intensity will, in addition, change owing to the absorption along the crystal. The axial evolution of the real pump beam radius can be described by

$$w_p(z) = r_p\sqrt{1 + \left(\frac{z - z_0}{r_p}\tan\theta_i\right)^2}, \tag{5.47}$$

where, r_p denotes the pump beam focal spot radius inside the crystal and z_0 the position of the focus. As the local pump efficiency depends on the local pump intensity, the effective pump beam radius can be described by the absorption-averaged beam radius along the crystal

$$w_{p,eff} = \frac{\int_0^L w_p(z)e^{-\alpha_p z}dz}{\int_0^L e^{-\alpha_p z}dz}. \tag{5.48}$$

Using these equations, the behaviour of a longitudinally-diode-pumped solid-state laser can be calculated in a simple way to a good approximation. In order to determine the optimum position of the focus, the minimum of $w_{p,eff}$ with respect to

z_0 has to be found. However, as Eq. (5.48) cannot be calculated analytically, this can only be solved numerically. Therefore, another possibility can be investigated, leading to an analytical solution: As the threshold depends on the square of the pump beam radius, another effective pump beam radius $w'_{p,eff}$ can be defined, the quadratic effective pump beam radius

$$w'_{p,eff} = \sqrt{\frac{\int_0^L w_p^2(z) e^{-\alpha_p z} dz}{\int_0^L e^{-\alpha_p z} dz}}. \tag{5.49}$$

As there is no root in the integral expression, the integrals can both be calculated analytically, resulting in

$$w'_{p,eff} = \sqrt{r_p^2 + \left[\frac{(z_0\alpha_p - 1)^2 + 1}{\alpha_p^2} - \frac{L^2 - 2Lz_0 + 2\frac{L}{\alpha_p}}{e^{\alpha_p L} - 1}\right] \tan^2 \theta_i}. \tag{5.50}$$

The minimum of this expression with respect to z_0 can be found easily. As the minimum of $w'_{p,eff}$ coincides with the minimum of $w'^2_{p,eff}$, we use

$$\frac{\partial w'^2_{p,eff}}{\partial z_0} = 0 \tag{5.51}$$

to find the minimum quadratic effective pump spot radius. This yields an optimum focus position of

$$z_{0,opt} = \frac{1}{\alpha_p} - \frac{1 - \eta_{abs}}{\eta_{abs}} L, \tag{5.52}$$

which approximately minimizes the threshold pump power. Thus, the approximate optimum focus position can be directly calculated from the laser medium parameters. It is surprisingly independent of the divergence angle θ_i and the pump spot diameter r_p.

A second pumping geometry especially suited for high power lasers or amplifier heads is transverse or side pumping, in which the laser diodes are aligned along the side of a laser rod. The pump radiation is then absorbed in a single transverse passage through the rod. This is of course, only possible and efficient for laser media which show a pump absorption length smaller than the rod diameter. This may be achieved using high-spectral-brightness laser diodes pumping the Nd^{3+} ion on its peak absorption, which allows this side-pumping. A sectional view of such a pump arrangement is shown in Fig. 5.13. A big challenge in this layout is the construction of the pump chamber and the complex water flow between the different diode heat sinks and the central flow tube around the laser crystal. As a result of the fact that the diode heat sinks are usually connected electrically in series, they exhibit a potential difference between each other and need to be electrically mutually insulated. As the cooling water, however, forms one closed circuit, one has to control the conductivity of the water, usually below 5 µS, in order to avoid electro corrosion between the different electrical potentials in the cooling circuit.

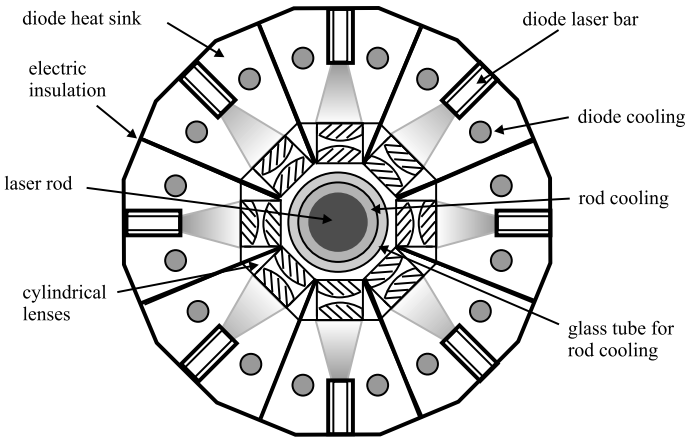

Fig. 5.13 Schematic setup of a transverse diode-pumped rod laser [3]

Recently, optical pumping at around 875 nm has become more and more popular, as this pump line directly excites the ions to the upper laser level. Thus no fast relaxation is necessary and the laser quantum efficiency is increased through reduction of the quantum defect. This results in a lower heat load per pump transition and thus in a higher laser output power, which can be reached before thermal effects become significant.

Applications

The Nd^{3+} laser, especially using the YAG host, is widely used in industry and research applications. In industry, the lasers are mostly used for marking and engraving applications, for spot welding and line welding as well as for hole drilling. In research the laser is mostly used as a high power pump source with high beam quality compared to laser diodes, either by using the laser radiation itself or by frequency doubling of the 1.064 µm line to 532 nm, which is an ideal pump for the Ti:sapphire laser, as discussed in Sect. 5.2.3.

5.2.2 The Tm^{3+}-Laser

The Tm^{3+} laser is a typical quasi-three-level laser operating around 1.9–2 µm. As an example, Fig. 5.14 shows the energy level scheme in three different hosts and Fig. 5.15 the corresponding emission and absorption cross sections for Tm^{3+}:YAG. The specialty of Tm^{3+} lasers is their unique pumping scheme allowing for the use of highly efficient ∼790 nm AlGaAs laser diodes for pumping. As an example, Fig. 5.16 shows the corresponding pump absorption cross section for Tm^{3+}:YAG. This is based on a **cross-relaxation process** $^3H_4 + {}^3H_6 \rightarrow 2 \times {}^3F_4$, which is very

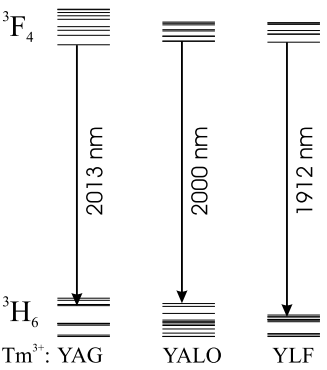

Fig. 5.14 Energy scheme of the Tm^{3+} ion in various hosts and the main laser transitions

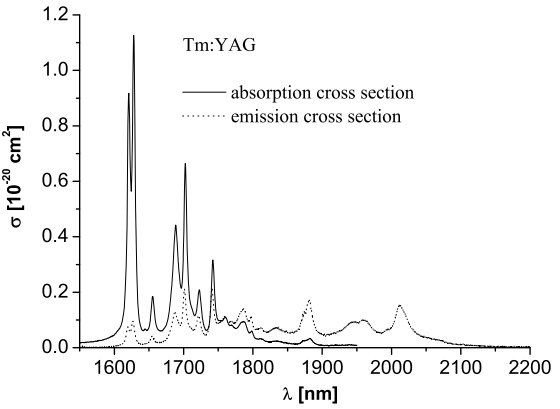

Fig. 5.15 Absorption and emission cross sections of Tm^{3+}:YAG around 2 µm

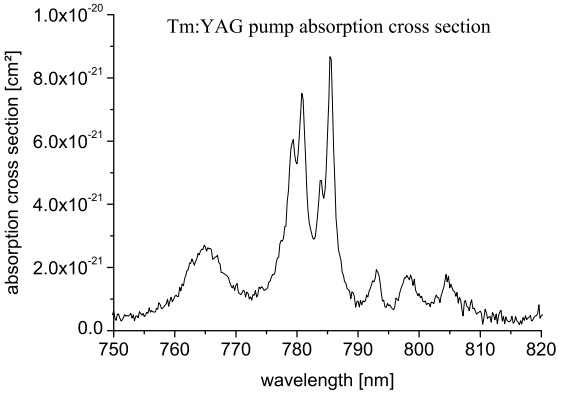

Fig. 5.16 Pump absorption cross section for Tm^{3+}:YAG

efficient in nearly all hosts. This process is shown in Fig. 5.17 on the example of a Tm^{3+}:YLF laser: The medium is pumped at a wavelength of 792 nm into the $^3H_4$ manifold. Owing to the close match in energy between the $^3H_4 - {}^3F_4$ transition and the $^3H_6 - {}^3F_4$ transition, the excited Tm^{3+} ion makes a transition to the $^3F_4$

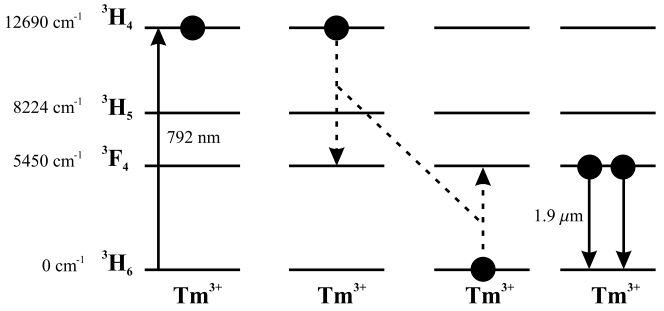

Fig. 5.17 Cross-relaxation process between two Tm^{3+} ions in YLF

manifold. This transition transfers the corresponding energy to a second, unexcited Tm^{3+} ion, which uses this energy to excite its $^3F_4$ manifold. Therefore, two excited ions in the upper laser manifold have been created by one absorbed pump photon. Thus, the number of extracted laser photons per absorbed pump photon, which is called **quantum yield**, can be greater than 100 % in Tm^{3+} lasers.

This process can, of course, also occur in the reverse direction, i.e. that of two Tm^{3+} ions in the $^3F_4$ manifold,from which one can make a transition to the ground-state manifold $^3H_6$, whilst transferring the generated energy to the other ion to excite it from the $^3F_4$ manifold into the $^3H_4$ manifold. This process is called **upconversion**.

Different Hosts for Thulium Lasers

Among the hosts presented in Table 5.1, YLF ($YLiF_4$) provides the highest fluorescence lifetimes and reasonable high pump absorption and laser emission cross-sections, shown in Fig. 5.18 and Fig. 5.19, resulting in low saturation intensities for efficient laser operation. As YLF is a birefringent laser host, different absorption and emission cross sections are needed depending on the polarization of the light with respect to the crystallographic axes. However, the relative re-absorption and thermal lower level population is higher than in YALO or YAG, as shown in Fig. 5.20. YALO, and especially YAG, on the other hand suffer from high saturation intensities. So high brightness pump diode systems are necessary to provide low threshold operation. For the two most important fiber materials, ZBLAN and silica, the spectroscopic data are summarized in Table 5.2. Owing to the very low phonon energy of ZBLAN the fluorescence lifetime is not strongly affected by multi-phonon relaxation. However, in silica the spontaneous lifetime τ_{sp} is about 4.75 ms, which is dramatically reduced by a strong multi-phonon relaxation. Whilst the saturation intensity of Tm^{3+}:ZBLAN is comparable with the ones presented for the crystalline hosts in Table 5.1, Tm^{3+}:silica shows a ten-fold higher saturation intensity compared with ZBLAN. Due to the amorphous nature of the glasses, the optical transitions are inhomogeneously broadened, resulting in broad absorption and emission bands. An example is given for ZBLAN glass in Fig. 5.21 for the laser transition and in Fig. 5.22 for the most important pump band. Also, in the glass media the cross-relaxation pumping is very efficient and results in high overall laser efficiencies.

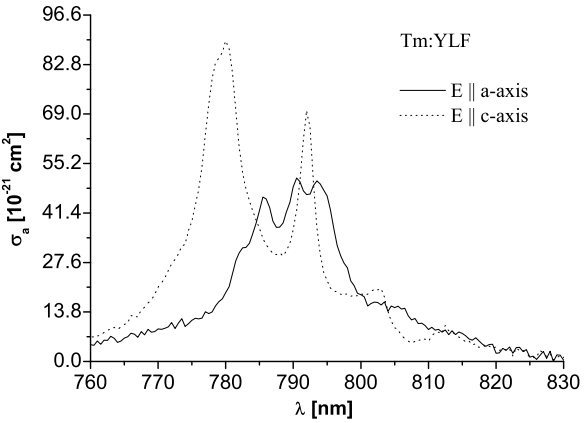

Fig. 5.18 Pump absorption cross section for Tm^{3+}:YLF

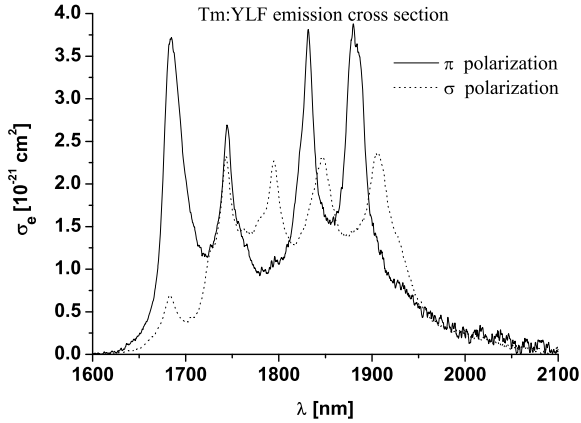

Fig. 5.19 Laser emission cross section for Tm^{3+}:YLF

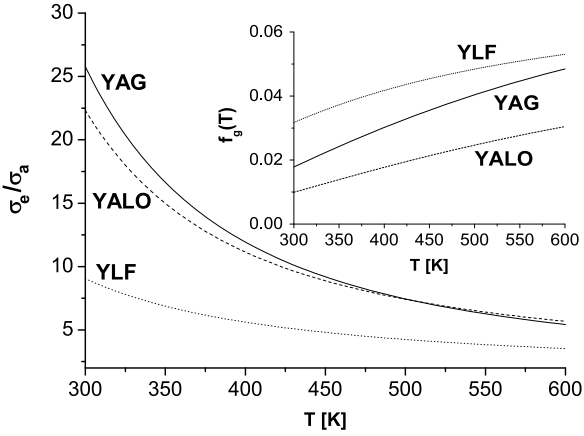

Fig. 5.20 Calculated emission-to-absorption cross-section ratio and lower laser level population of Tm^{3+} in different hosts as a function of the crystal temperature

Table 5.1 Important data on Tm^{3+}-doped laser hosts. Some data are taken from [5–9]

Host crystal	YAG	YALO	YLF
$^3F_4$ levels [cm^{-1}]	5556, 5736, 5832, 5901, 6041, 6108, 6170, 6224, 6233	5622, 5627, 5716, 5722, 5819, 5843, 5935, 5965	5605, 5757, 5757, 5760, 5827, 5944, 5967, 5967, 5977
$f_{u,0}$	0.459	0.228	0.286
τ_f [ms]	10.5	5.0	15.6
$^3H_6$ levels [cm^{-1}]	0, 27, 216, 241, 247, 252, 588, 610, 690, 730	0, 3, 65, 144, 210, 237, 271, 282, 313, 440, 574, 628, 628	0, 31, 31, 56, 282, 310, 324, 327, 327, 374, 375, 375, 409
$f_{g,(i)}$	0.018 (6)	0.010 (12)	0.032 (9)
λ_s [nm]	2013	2000	1912
$\sigma_e(\lambda_s)$ [10^{-21} cm^2]	1.53	5.0	4.0 (π)
$\frac{\sigma_e(\lambda_s)}{\sigma_a(\lambda_s)}$	25.8	22.3	9.05
I^s_{sat} [kW/cm^2]	5.91	3.80	1.50
$^3H_4$ levels [cm^{-1}]	12607, 12679, 12747, 12824, 12951, 13072, 13139, 13159	12515, 12574, 12667, 12742, 12783, 12872, 12885, 12910, 12950	12621, 12621, 12644, 12644, 12741, 12825, 12831, 12831, 12831
λ_p [nm]	786	795	792
$\sigma_{a,p}(\lambda_p)$ [10^{-21} cm^2]	8.67	7.5	4.0 (σ), 6.0 (π)
$\frac{\sigma_{e,p}(\lambda_p)}{\sigma_{a,p}(\lambda_p)}$	0.63	1.05	0.88
I^p_{sat} [kW/cm^2]	15.1	9.57	3.62

Table 5.2 Spectroscopic data on Tm^{3+}-doped glasses. Some data are taken from [2, 4]

Host glass	ZBLAN	Silica
τ_f [ms]	10.9	0.34
λ_s [nm]	1940	1970
$\sigma_e(\lambda_s)$ [10^{-21} cm^2]	0.93	2.6
$\frac{\sigma_e(\lambda_s)}{\sigma_a(\lambda_s)}$	23.6	32.3
I^s_{sat} [kW/cm^2]	9.69	110.6
λ_p [nm]	791	790
$\sigma_{a,p}(\lambda_p)$ [10^{-21} cm^2]	3.25	9.93
$\frac{\sigma_{e,p}(\lambda_p)}{\sigma_{a,p}(\lambda_p)}$	1.44	~1
I^p_{sat} [kW/cm^2]	23.8	276
E_P^{max} [cm^{-1}]	590	1100

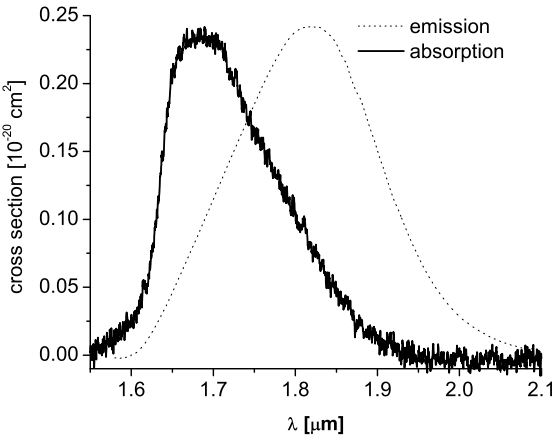

Fig. 5.21 Absorption and emission cross sections of Tm^{3+}:ZBLAN around 2 μm

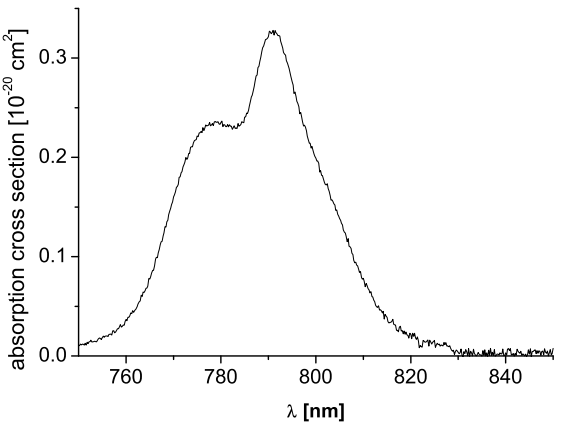

Fig. 5.22 Pump absorption cross section of Tm^{3+}:ZBLAN around 790 nm

The following section gives an overview over energy-transfer processes and its descriptions.

Energy-Transfer Processes

Fast energy-transfer rates are of the order of 10^7 s^{-1}, whilst the interaction between the active ion and the host phonons occurs at a much faster rate on the order of 10^{11} s^{-1} [10]. Therefore, energy transfer can be seen as an incoherent process and Fermi's golden rule may be applied to the interaction Hamiltonian between the interacting electrons of the donor ion (index D) and the acceptor ion (index A), given by

$$\mathbb{H}_{DA} = \frac{1}{2\kappa} \sum_{i,j} \frac{e^2}{| \vec{r}_i^{\,D} - \vec{r}_j^{\,A} |}. \tag{5.53}$$

This corresponds to an interaction that is caused by the electric or magnetic field of the ions, with the electric field contribution being several orders of magnitude

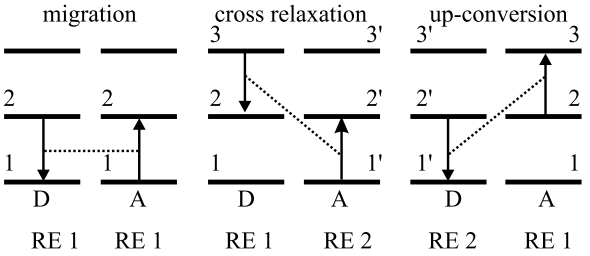

Fig. 5.23 Most important energy-transfer processes in which donor D and acceptor A can be the same or different ion species (denoted by the rare-earth ions RE 1 or RE 2)

stronger than that of the magnetic field contribution [11]. Here, $\vec{r}$ are the positions of the electrons in ions D and A, κ is related to the polarizability of the medium and the sum is over all electrons in the corresponding ion [14]. Applying Fermi's golden rule and a multipole expansion of the interaction Hamiltonian results in an interaction rate [15, 17]

$$W_{DA} = \frac{C^{dd}}{R^6} + \frac{C^{dq}}{R^8} + \frac{C^{qq}}{R^{10}} + \cdots, \tag{5.54}$$

in which R is the distance between the two ions and the different constants C represent dipole-dipole (dd), dipole-quadrupole (dq) and quadrupole-quadrupole (qq) contributions. As long as the ion spacings R are not too small, the first term in Eq. (5.54) dominates. The interaction lengths may then correspond to several nm [15, 16]. A second interaction mechanism can be caused by the direct overlap between the electronic wave functions of the donor ions and the acceptor ions [18–20]; however, this may only occur at very short inter-ionic distances between the donor and the acceptor, and therefore, only for extremely high dopant concentrations. A special case of this energy-transfer process is the super-exchange, where, the donor and acceptor wave functions overlap not directly, but both overlap with an intermediate ligand ion [21].

For the dipole-dipole interaction, the coupling parameter was shown to be linked to the overlap between the donor emission cross section $\sigma_e^D(\lambda)$ and the acceptor absorption cross section $\sigma_a^A(\lambda)$ by Dexter [17]

$$C_{DA}^{dd} = \frac{9\chi^2 c}{16\pi^4 n^2} \int \sigma_e^D(\lambda)\sigma_a^A(\lambda)d\lambda. \tag{5.55}$$

Therein, $\chi^2 \sim \frac{2}{3}$ accounts for an orientational average.

Whilst this approach deals with the microscopic interaction between two ions, it is important to have a description of the macroscopic behaviour of an active medium in order to model its excitation processes. The most important energy-transfer processes occurring in rare earth doped solid-state materials are shown in Fig. 5.23. They are migration, cross relaxation and upconversion. Migration is the energy transfer between ions of the same species involving the same transition levels in both ions, called donor-donor transfer. Thus, the corresponding coupling parameter is given by

$$C_{DD} = \frac{3c}{8\pi^4 n^2} \int \sigma_e(\lambda)\sigma_a(\lambda)d\lambda \tag{5.56}$$

by analogy with Eq. (5.55). Here, $\sigma_e(\lambda)$ and $\sigma_a(\lambda)$ are the absorption and emission cross sections of the same transition between two manifolds. Three types of migration may be distinguished, depending on the relative strength of the donor-donor and donor-acceptor coupling parameters: diffusion, fast migration and super-migration.

In the case of $C_{DD} \ll C_{DA}$, the migration can be described by a diffusion process [22], resulting in a macroscopic de-excitation rate of the donors of

$$\frac{\partial N_D}{\partial t} = -\frac{16\pi^2}{3}\left(\frac{1}{2}\right)^{\frac{3}{4}} C_{DA}^{\frac{1}{4}} C_{DD}^{\frac{3}{4}} N_D^0 N_D N_A, \tag{5.57}$$

where N_D^0 is the total density of donors that can contribute to the migration process, N_D the density of excited donors and N_A the density of acceptors. This macroscopic rate is valid for long times given by [12]

$$t > \frac{16\pi^3}{9}\frac{C_{DA}}{W_{DA}^2} N_A^2 \approx \frac{16\pi^3}{9}\frac{R_{DA}^{12}}{C_{DA}} N_A^2, \tag{5.58}$$

with R_{DA} being the donor-acceptor distance.

The fast migration ($C_{DD} \gg C_{DA}$) is often the dominant process with donor-donor coupling parameters C_{DD} that are some orders of magnitude larger than those for the donor-acceptor energy transfer C_{DA} given by Eq. (5.55). This can be explained as the donor-acceptor interaction depends on two different transitions, which need to overlap spectrally to yield a large energy-transfer parameter, whilst the donor-donor interaction relies upon the same transition, so the overlap is guaranteed by Eq. (2.32). In the case of fast migration, a donor excitation can migrate significantly before it interacts with an acceptor, thus increasing the macroscopic probability for the donor-acceptor transfer processes to occur. Whenever $C_{DD} \geq C_{DA}$, the macroscopic de-excitation rate can be described by the hopping model [23], resulting in

$$\frac{\partial N_D}{\partial t} = -\pi\left(\frac{2\pi}{3}\right)^{\frac{5}{2}} \sqrt{C_{DA} C_{DD}}\, N_D^0 N_D N_A \tag{5.59}$$

for long times as given by Eq. (5.58). In the case of upconversion ($N_D^0 = N_{RE2}$, $N_D = N_{2'}$ and $N_A = N_2$) this rate equation is often rewritten as

$$\frac{\partial N_{2'}}{\partial t} = -k_{up} N_2 N_{2'} \tag{5.60}$$

with

$$k_{up} = \pi\left(\frac{2\pi}{3}\right)^{\frac{5}{2}} \sqrt{C_{DA}^{up} C_{DD}^{up}}\, N_{RE2}, \tag{5.61}$$

$$C_{DA}^{up} = \int \sigma_{2'\to 1',e}(\lambda)\sigma_{2\to 3,a}(\lambda)d\lambda, \tag{5.62}$$

$$C_{DD}^{up} = \int \sigma_{2'\to 1',e}(\lambda)\sigma_{1'\to 2',a}(\lambda)d\lambda, \tag{5.63}$$

whilst for cross relaxation ($N_D^0 = N_{RE1}$, $N_D = N_3$ and $N_A = N_{1'}$) one often finds that

$$\frac{\partial N_3}{\partial t} = -k_{cr} N_{1'} N_3 \tag{5.64}$$

with

$$k_{cr} = \pi \left(\frac{2\pi}{3}\right)^{\frac{5}{2}} \sqrt{C_{DA}^{cr} C_{DD}^{cr}} N_{RE1}, \tag{5.65}$$

$$C_{DA}^{cr} = \int \sigma_{3\to 2,e}(\lambda)\sigma_{1'\to 2',a}(\lambda)d\lambda, \tag{5.66}$$

$$C_{DD}^{cr} = \int \sigma_{3\to 1,e}(\lambda)\sigma_{1\to 3,a}(\lambda)d\lambda. \tag{5.67}$$

Upconversion and cross relaxation are reverse processes on the microscopic scale, which are thermodynamically linked to each other. Using Eqs. (2.32), (5.55) the relation

$$\frac{C_{DA}^{cr}}{C_{DA}^{up}} = \frac{\int \sigma_{3\to 2,e}(\lambda)\sigma_{1'\to 2',a}(\lambda)d\lambda}{\int \sigma_{2'\to 1',e}(\lambda)\sigma_{2\to 3,a}(\lambda)d\lambda} = \frac{Z_{2'} Z_2}{Z_{1'} Z_3} \tag{5.68}$$

can be deduced as the ratio of the microscopic transfer parameters. It depends only on the partition functions Z_i of the involved manifolds. In the special, but most important case, in which RE 1 and RE 2 are the same ion species, this expression simplifies to

$$\frac{C_{DA}^{cr}}{C_{DA}^{up}} = \frac{\int \sigma_{3\to 2,e}(\lambda)\sigma_{1\to 2,a}(\lambda)d\lambda}{\int \sigma_{2\to 1,e}(\lambda)\sigma_{2\to 3,a}(\lambda)d\lambda} = \frac{Z_2^2}{Z_1 Z_3} \tag{5.69}$$

As a result of the principal difference between the migration processes in upconversion and cross relaxation, such a simple relation cannot be set up for the rate-equation parameters k_{cr} and k_{up}. However, it can be shown from the equations above that

$$\frac{k_{cr}}{k_{up}} = \frac{N_{RE1}}{N_{RE2}} \frac{Z_{2'}}{Z_{1'} Z_3} \sqrt{Z_1 Z_2 \frac{\int e^{-\frac{hc}{k_B T\lambda}} \sigma_{1\to 3,a}^2(\lambda)d\lambda}{\int e^{-\frac{hc}{k_B T\lambda}} \sigma_{1'\to 2',a}^2(\lambda)d\lambda}}, \tag{5.70}$$

and for the case of identical species this simplifies to

$$\frac{k_{cr}}{k_{up}} = \frac{Z_2}{Z_3} \sqrt{\frac{Z_2}{Z_1} \frac{\int e^{-\frac{hc}{k_B T\lambda}} \sigma_{1\to 3,a}^2(\lambda)d\lambda}{\int e^{-\frac{hc}{k_B T\lambda}} \sigma_{1\to 2,a}^2(\lambda)d\lambda}}. \tag{5.71}$$

The regime of super-migration is reached when the actual acceptor concentration c_A, i.e. the probability of occupation of a possible lattice site by an acceptor, exceeds the critical concentration c^*,

$$c_A > c^* = \left(\frac{C_{DA}}{C_{DD}}\right)^{\frac{1}{8}}. \tag{5.72}$$

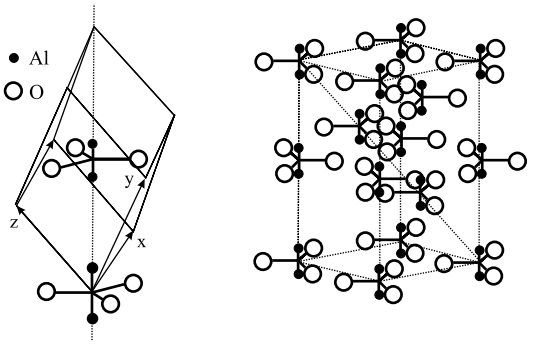

Fig. 5.24 Atomic structure of the Al_2O_3 host crystal [28]

Owing to $c_A < 1$ the super-migration can only occur for $C_{DD} > C_{DA}$. Then the fast migration distributes the energy over all donors before the donor-acceptor transfer can occur.

It has to be noted that even if the absorption and emission spectra in Eq. (5.55) do not overlap, an energy-transfer process may still exist for this transition; provided the excess energy that would be needed to make the cross sections overlap is compensated for by the emission or absorption of a lattice phonon [24–27].

5.2.3 The Ti^{3+}:Al_2O_3 Laser

In contrast to the two solid-state lasers discussed before, which are examples of rare-earth-ion-based laser media, the Ti^{3+}:sapphire laser (Ti^{3+}:Al_2O_3) uses the trivalent transition-metal titanium ion as the active ion. The host medium is single-crystalline aluminum oxide Al_2O_3, the same host as used in the first laser, the ruby laser (Cr^{3+}:Al_2O_3). In this context, it should be noted that the name "Ti^{3+}:sapphire laser" is tautological, as "sapphire" is already the name for Ti^{3+}-doped aluminum oxide, just as "ruby" denotes the Cr^{3+}-doped aluminum oxide. Thus, one could also speak of the "sapphire laser" itself. In the following, we will discuss the special energy structure and the resulting laser properties arising from the transition-metal nature of the active ion, as well as some applications of the Ti^{3+}:Al_2O_3 laser.

The Laser Medium

Being a 3*d* transition metal, the Ti^{3+} ion exhibits a single 3*d* electron in its outer shell, which is the "active laser" electron. The free ion is thus similar to a hydrogen atom and higher-lying electronic states cannot be excited by the energies accessible during optical pumping. The whole pump and laser process thus takes place between the different levels that are created by the splitting of the five-fold-degenerate free-ion ground state ^2D in the host matrix. This host matrix is shown in Fig. 5.24.

In contrast to the splitting scheme discussed in Fig. 2.3 for the rare-earth ions, the optically active electron here is not shielded from the crystal field. This causes

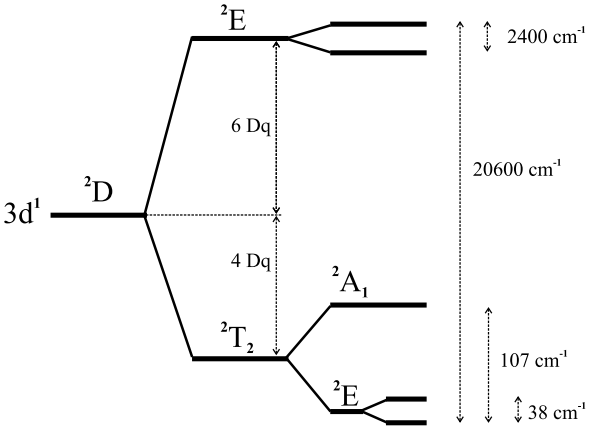

Fig. 5.25 Energy level diagram of the crystal-field splitting of the Ti^{3+} ion in Al_2O_3 [28]

a crystal-field splitting which dominates the spin-orbit splitting. Whilst the actual energy of this splitting is, of course, a host- and ion-dependent value, the theoretical description of the strong-crystal-field splitting can be generalized. In this perturbational description, the scale of the splitting energy is given by the parameter product Dq, in which

$$D = \frac{1}{4\pi\epsilon_0}\frac{35}{4}\frac{Ze^2}{a^5} \tag{5.73}$$

accounts for the strength of the crystal field, caused by the charge of the ligand $-Ze$ at a distance a from the central ion, and

$$q = \frac{2}{105}\langle 3d|r^4|3d\rangle \tag{5.74}$$

is proportional to the quantum-mechanical radial integral of the $3d$ wave functions that has to be calculated to obtain the energy difference. The ground-state splits by a total amount of $10Dq$, for which the ratio between the amount of energy decrease of the lower state and the amount of increase of the upper state depends on the symmetry of the external ligand ions and the resulting degeneracy of the final levels. In the case presented here, there are the six oxygen ions around the Ti^{3+} ion, resulting in an octahedral coordination, causing a splitting into a doubly-degenerate ^2E state and a triply-degenerate $^2T_2$-state. As the total energy change of the splitting needs to be zero, the ^2E state is raised $6Dq$ above the initial, free-ion ground state, whilst the $^2T_2$-state is lowered by $4Dq$ with respect to the initial ground state as shown in Fig. 5.25. As these octahedra are trigonally distorted, as can be seen in Fig. 5.24, the $^2T_2$-state is split further. The ^2E excited state degeneracy is also lifted by the so called **Jahn-Teller effect**, which states that the degeneracy of an electronic state in a non-linear complex will be lifted by a spontaneous deformation of the surrounding lattice. However, strictly speaking, no optical dipole transitions should occur between these states as they all have even parity. The fact that there are optical dipole transitions is a direct result of the breaking of inversion symmetry as soon as an Al^{3+} ion is replaced by a Ti^{3+} ion. This causes a mixing of the odd-parity wave

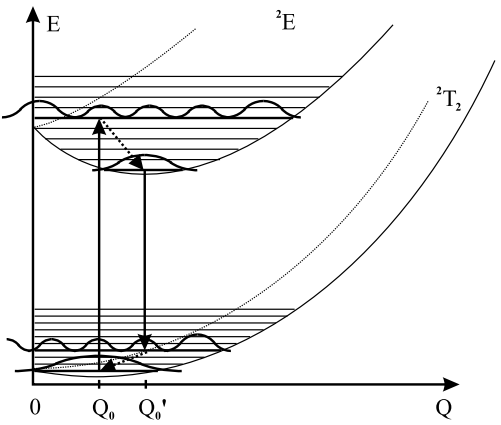

Fig. 5.26 Energy level diagram showing the electron-phonon coupling of the Ti^{3+} ion in Al_2O_3 [28]

functions of the oxygen ions with those on the Ti^{3+} ion, allowing optical-dipole transitions within the split ground state.

Up to this point, there is no principle difference of this energy scheme with the ones discussed for the rare-earth ions. However, the energy levels here are a direct consequence of the crystal field, and thus, of the spatial positions of the oxygen ions in the crystal lattice. Their energies are therefore very sensitive to this configuration. The phonons of the host crystal now cause vibrations of the oxygen ions and thus a modulation of the crystal field, which will have an influence on to the energies of those levels. Quantum-mechanically, this strong electron-phonon coupling results in so-called **vibronic states**, mixed states between the electronic states of the ion and the phonon states of the lattice. They can be described by the **configurational coordinate model**. In this model, the energy of the levels is plotted as a function of the configurational coordinate Q, which can be seen as a parameter describing the distance of the oxygen atoms of the vibrating octahedra with respect to the Ti^{3+} ion. In this description, the energy variation of a level can be described for small changes in configuration by a parabolic potential as shown in Fig. 5.26, and thus at each level, a harmonic oscillator can be assumed. For the ground state, this results in three paraboloids oriented around the origin $Q = 0$, from which Fig. 5.26 shows a cut along one radial Q-axis through the minimum of one of the paraboloids. For the excited state, two paraboloids result, which are also shifted outward from the origin $Q = 0$. As the Jahn-Teller effect is different for the ground and the excited state, it causes a different lattice distortion, and thus, the corresponding configurational coordinate of the parabola minimum Q_0 and Q_0' is also different. Taking into account that the transition probability depends on the overlap of the wave functions, which are also indicated in Fig. 5.26, a strong wavelength shift exists between absorption and emission. This is called **Franck-Condon shift**. After the absorption process, the excitation will quickly thermalize within the upper harmonic oscillator levels owing to the strong interaction with the phonons, which created these levels. Thus, the emission process with the highest probability will start from the lowest levels in the excited state. However, from this state only transitions to higher states

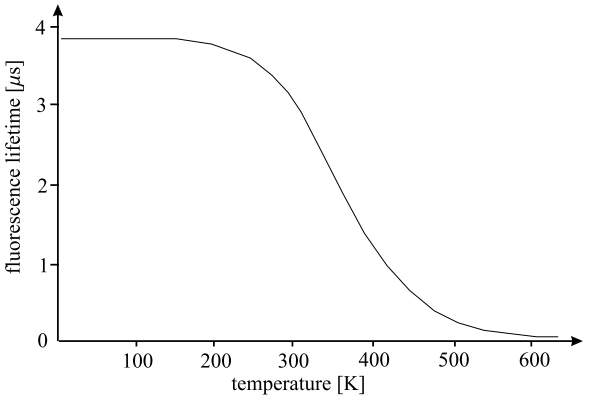

Fig. 5.27 Upper-state fluorescence lifetime of the Ti^{3+} ion in Al_2O_3 as a function of the temperature [28]

within the ground-state parabola yield a high overlap in wavefunction, as the coordinates of the minima are different (**Franck-Condon principle**). This causes the strong wavelength shift between absorption and emission.

A second effect of the vibronic states is the large fluorescence bandwidth, and thus, the tunability of the Ti^{3+}:Al_2O_3 laser. Owing to the spatially oriented three paraboloids in the ground state, a transition from an excitation at a fixed coordinate Q can occur towards a huge number of possible final states and phonon energies in the ground state.

The Ti^{3+}:Al_2O_3 laser crystals are grown by the Czochralski method. In contrast to Nd^{3+}:YAG, where the dopant concentration is limited by the ionic radius of the neodymium ion to approximately 1 %, or compared with Tm^{3+}:YAG, in which the thulium ion concentration can reach several 10 %; the Al_2O_3 crystal can only be doped with Ti^{3+} on the order of 0.1–0.25 %. One reason for this low concentration is the higher ionic radius of Ti^{3+} (0.067 nm) compared with Al^{3+} (0.053 nm), the other reason can be related to the Jahn-Teller effect, as a higher doping concentration would cause a ground-state degeneracy, which itself would result in a Jahn-Teller splitting, creating a lattice deformation that is not compatible with the Al_2O_3 lattice.

Laser Parameters

The lifetime of the Ti^{3+}:Al_2O_3 fluorescence at room temperature is around 3.1 µs, and thus three orders of magnitude shorter than the fluorescence lifetimes of many rare-earth doped crystals, such as those using Tm^{3+}, Ho^{3+} or Er^{3+} as the active ion. Owing to the electron-phonon coupling, this lifetime strongly depends on the crystal temperature as shown in Fig. 5.27. As the optical transitions are a result of the statically broken inversion symmetry, mixing odd-parity wave functions into the ground state, and not a result of the vibronic states, the spontaneous optical emission rate τ_{sp}^{-1} is temperature independent. However, also non-radiative transitions from the excited state into the ground state exist. These relaxation transitions show a rate τ_r^{-1}, resulting in a total fluorescence lifetime of

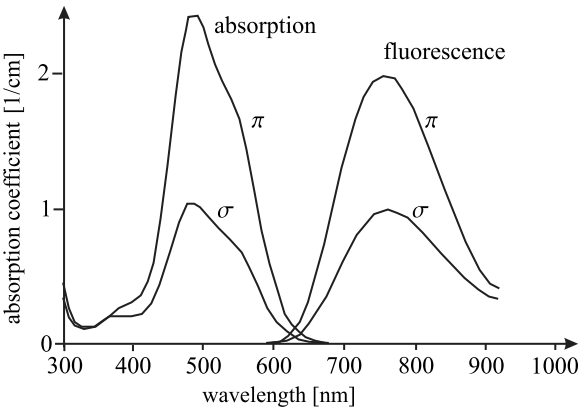

Fig. 5.28 Absorption coefficient of a 0.1 %-by-weight-doped Ti^{3+}:Al_2O_3 crystal and its fluorescence intensity for the polarizations parallel (π) and perpendicular (σ) to the c-axis [28]

$$\tau_{tot}^{-1} = \tau_{sp}^{-1} + \tau_r^{-1}. \tag{5.75}$$

This relaxation rate is strongly temperature dependent and is caused by a tunneling of the upper level excitations in the ^2E parabolas into the ground-state parabolas. As the energy gap (tunnel distance) is smaller for highly excited levels, the increasing fractional excitation of the higher levels in the ^2E parabolas with temperature causes a strong increase in the non-radiative transition rate. As can be seen from Fig. 5.27, this process starts at a temperature around 200 K and then quickly reduces the fluorescence lifetime for higher temperatures. The quantum yield of the laser at room temperature, which is the amount of fluorescence photons with respect to the total amount of transitions, thus results in

$$\eta_{QY} = \frac{\tau_{tot}(300\ \mathrm{K})}{\tau_{sp}} = \frac{3.1\ \mu\mathrm{s}}{3.85\ \mu\mathrm{s}} = 0.8. \tag{5.76}$$

The fluorescence of Ti^{3+}:Al_2O_3 is a maximum for light polarized parallel to the crystallographic c-axis as shown in Fig. 5.28 together with the absorption coefficient. This results in a peak emission cross section for this polarisation of 3.5×10^{-19} cm^2 at 795 nm, which has been determined from its fluorescence spectrum using the Füchtbauer-Ladenburg relation Eq. (1.77) in Fig. 5.29. It can be clearly seen that the emission cross section is shifted towards lower wavelengths with respect to the fluorescence. The absorption band is very broad, resulting in a large variety of possible pump sources. Whilst in the past mainly Ar^+ ion lasers at 514 nm have been used as a pump, today, frequency-doubled Nd^{3+}:YAG, Nd^{3+}:YVO_4 or Nd^{3+}:YLF lasers are used owing to their much higher efficiency compared with the Ar^+ laser. Also pulsed pumping by flashlamps is possible, however, as a result of the short upper level lifetime, high pump intensities and short pump pulses are necessary, which needs specially designed low-inductance flashlamp circuits and flashlamps for high operation lifetime. Especially the flashlamp design is critical when it comes to high pump energies of several 100 J as the short pulse width on the order of 2–10 µs also corresponds to a low flashlamp explosion energy, see Eq. (5.8).

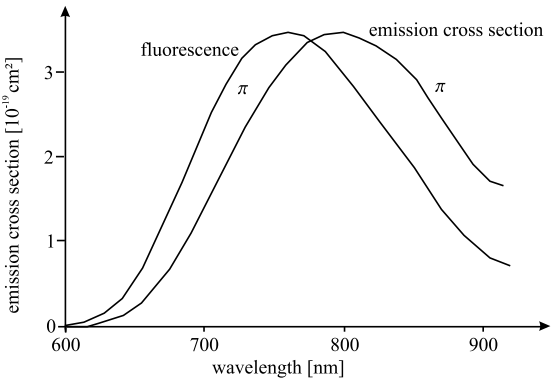

Fig. 5.29 Emission cross section and fluorescence intensity of a Ti^{3+}:Al_2O_3 crystal for the polarization parallel (π) to the c-axis [28]

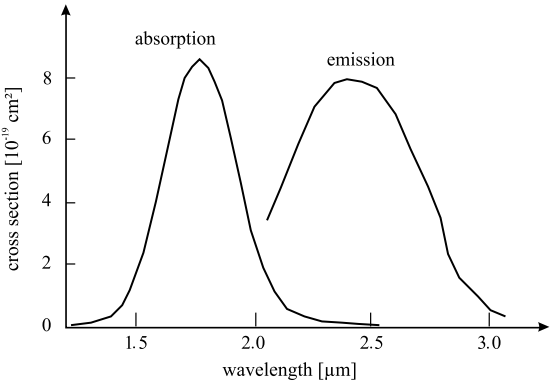

Fig. 5.30 Absorption and emission cross sections of Cr^{2+}:ZnSe [29]

Applications

The main application of the Ti^{3+}:Al_2O_3 laser today arises from its large tuning and amplification range. It is the generation of ultra-short pulses, already discussed in Sect. 4.2, as well as the amplification of ultra-short pulses discussed in Sect. 4.2.3, where these lasers are dominant. Another important application is in spectroscopy, to generate broadly-tunable radiation with a small linewidth. Similar spectral properties can be achieved with Cr^{3+}:$LiSrAlF_6$ and Cr^{3+}:$LiCaAlF_6$, which show an emission band shifted towards the infrared compared with Ti^{3+}:Al_2O_3. However, the fluoride crystals are hygroscopic, which is a drawback for efficient cooling of the laser rods. A comparable laser medium in the 2.3 μm region is Cr^{2+}:ZnSe, which shows a broad emission range at 2–3 μm, as shown in Fig. 5.30. This allows the generation and amplification of ultra-short pulses in the mid-infrared spectrum.

5.3 Special Realisations of Lasers

In the following section we will investigate two of the most important laser geometries today, which are the fiber laser and the thin-disk laser. Both of these laser archi-

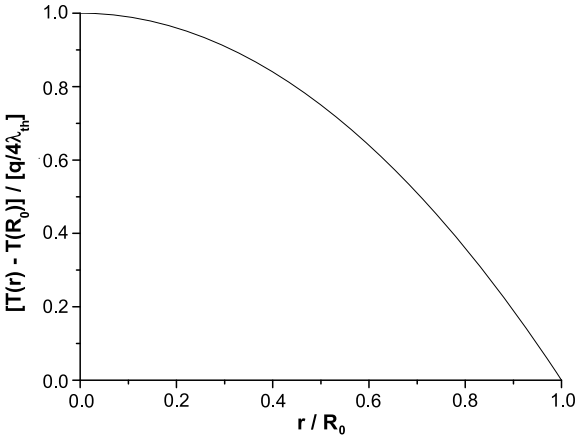

Fig. 5.31 Radial temperature profile in a homogeneously-heated, surface-cooled laser rod

tectures attempt to solve the main problematic issue in solid-state lasers: the thermal management of the laser medium. In standard rod lasers as discussed above, the heat dissipated inside the laser medium has to be extracted through the outer crystal surface, and a temperature profile will result from the finite heat transfer coefficient of the laser medium. This profile can be calculated from the heat-transfer equation [3]

$$\frac{\partial^2 T}{\partial r^2} + \frac{1}{r}\frac{\partial T}{\partial r} = \frac{q}{\lambda_{th}}, \tag{5.77}$$

assuming a cylindrical symmetry, where, $T(r)$ is the rod temperature,

$$q = \frac{P_{therm}}{\pi R_0^2 L} \tag{5.78}$$

the volumetric heat load, L the length of the rod, P_{therm} the power dissipated as heat in the medium and λ_{th} the heat-transfer coefficient of the medium. In the case of a homogeneous heat load q, this results in a parabolic temperature profile

$$T(r) = T(R_0) + \frac{q}{4\lambda_{th}}\left(R_0^2 - r^2\right), \tag{5.79}$$

with R_0 being the radius of the rod and $T(R)$ the temperature on the outer crystal surface. This temperature profile is shown in Fig. 5.31 and has two important influences on the laser medium, which are discussed in the following section.

5.3.1 Thermal Lensing and Thermal Stress

Thermal Lensing

As the index of refraction of the laser medium is usually temperature dependent, this temperature profile with the gain medium will create a refractive index distribution

resulting in the formation of a **thermal lens**. The corresponding index distribution is given by

$$n(r) = n_0 + \frac{\partial n}{\partial T}\big(T(r) - T(R_0)\big), \tag{5.80}$$

wherein $n_0 = n(R_0)$ is the refractive index of the rod at the surface. The thermal lens can have a positive or negative focal length depending on the sign of the thermal index coefficient $\frac{\partial n}{\partial T}$ of the laser medium. YAG, for example, has $\frac{\partial n}{\partial T} = 9.9 \times 10^{-6}\ \mathrm{K}^{-1}$ and thus a positive thermal lens, whilst, for example YLF, with $\frac{\partial n}{\partial T} = -2 \times 10^{-6}\ \mathrm{K}^{-1}$ for a polarization along the a-axis, shows a negative, i.e. diverging, thermal lens. Taking into account that a parabolic index profile

$$n(r) = n_0 - \frac{1}{2} n_2 r^2, \tag{5.81}$$

which is constant in axial direction along a (rod) length L, acts like a lens with a focal length of

$$f = \frac{1}{n_2 L}, \tag{5.82}$$

we obtain for the thermal lens

$$f_{th} = \frac{2\lambda_{th}\pi R_0^2}{\frac{\partial n}{\partial T} P_{therm}}, \tag{5.83}$$

where, it has to be taken into account that Eq. (5.82) is only valid for $f \gg L$. In some laser media, such as ZnSe or $YAlO_3$ (YALO), the thermal lensing can be strong enough that focal lengths shorter than the rod may result, especially for long crystals. But this is usually connected simultaneously to a very strong beam quality degradation as a result of aberrations caused by the non-parabolic temperature profile, and is therefore avoided in most lasers.

However, the measured values of thermal lenses differ from the simple relation in Eq. (5.83), because additional effects have to be considered: We also have to take into account that the rod will show a local thermal expansion, which will create a thermal stress. This stress itself causes an additional change in the refractive index by the **photoelastic effect**. All these material dependent effects can, however, be summed into one parameter ξ. For isotropic laser media such as YAG, the focal length of the total thermal lens can be expressed by

$$f_{th} = \frac{\pi R_0^2}{\xi P_{therm}}. \tag{5.84}$$

For YAG, a value of $\xi = 5.09 \times 10^{-7}\ \frac{\mathrm{m}}{\mathrm{W}}$ has been measured.

Finally, we have to take into account that the total thermal expansion will cause a bulging of the end faces of the rod, which itself is a positive contribution to the total thermal lens. This effect depends on the length of the crystal and results in a modified parameter [3]

$$\xi' = \xi + \frac{\alpha_{th} R_0 (n_0 - 1)}{\lambda_{th} L}, \tag{5.85}$$

which replaces the ξ in Eq. (5.84), where, α_{th} is the coefficient of thermal expansion of the medium.

In designing a laser resonator, the formation of a thermal lens has to be taken into account in order to maintain performance over an extended period. However, from the power dependence of the thermal lens it directly follows that in a laser with a medium that is affected by strong thermal lensing, the resonator has to be calculated and optimized for the operation point of the laser, i.e. for a certain thermal lens that will build up at the nominal pump and output power of the laser. A direct result of thermal lensing will mean that the laser is designed for a certain pump power only. The use of differing pump powers will cause a change in the laser mode size and waist position inside the resonator, and therefore, will lead to a varying overlap with the pump beam. Therefore, the laser slope efficiency can depend on the pump power. Also the true laser threshold can be different from the theoretical one, as with thermal lensing the threshold depends also on the stability range of the cavity, which becomes pump-power dependent.

Thermal Stress

In an actively cooled laser rod the inner volume has a higher temperature, and therefore, a larger thermal expansion than the outer part of the rod. This results in the formation of mechanical stresses. In a cylindrical laser rod, the stresses in radial, tangential and axial (z-axis) direction can be calculated from the temperature distribution in the plain strain approximation, which is valid for long, surface cooled laser media. This results in [49]

$$\begin{aligned}
\sigma_r(z,r) &= \frac{\alpha_T E}{1-\nu}\left(\frac{1}{R^2}\int_0^{R_0} T\left(z,r'\right)r'dr' - \frac{1}{r^2}\int_0^{r} T\left(z,r'\right)r'dr'\right)\\
\sigma_t(z,r) &= \frac{\alpha_T E}{1-\nu}\left(\frac{1}{R^2}\int_0^{R_0} T\left(z,r'\right)r'dr' + \frac{1}{r^2}\int_0^{r} T\left(z,r'\right)r'dr' - T(r,z)\right) \qquad (5.86)\\
\sigma_z(z,r) &= \sigma_r(z,r)+\sigma_t(z,r) = \frac{\alpha_T E}{1-\nu}\left(\frac{2}{R^2}\int_0^{R_0} T\left(z,r'\right)r'dr' - T(z,r)\right),
\end{aligned}$$

with σ_r, σ_t and σ_z being the radial, tangential and axial stress components, respectively, E being Young's modulus, ν Poisson's ratio, α_{th} the thermal expansion coefficient and R the radius of the rod. The equation for σ_z is valid for a laser medium where the ends are free to move. Inserting the temperature distribution from Eq. (5.79) for the homogeneously heated laser rod, we obtain

$$\sigma_r = \frac{\alpha_T E}{16\lambda_{th}(1-\nu)} q\left(r^2 - R_0^2\right) = \sigma_0\left(r^2 - R_0^2\right), \qquad (5.87)$$

$$\sigma_t = \frac{\alpha_T E}{16\lambda_{th}(1-\nu)} q\left(3r^2 - R_0^2\right) = \sigma_0\left(3r^2 - R_0^2\right), \qquad (5.88)$$

$$\sigma_z = \frac{\alpha_T E}{8\lambda_{th}(1-\nu)} q\left(2r^2 - R_0^2\right) = 2\sigma_0\left(2r^2 - R_0^2\right). \qquad (5.89)$$

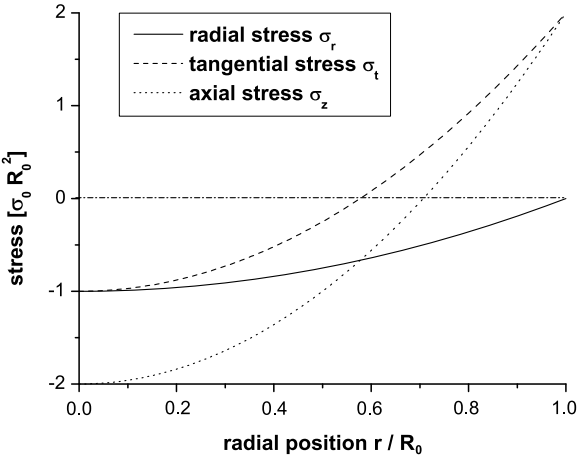

Fig. 5.32 Stress components in a homogeneously-heated, surface-cooled laser rod

Table 5.3 Thermal-shock parameter of several laser media [3]

Host crystal	YAG	GSAG	Al_2O_3	SiO_2 glass
R_s	7.9 $\frac{W}{cm}$	6.5 $\frac{W}{cm}$	100 $\frac{W}{cm}$	1 $\frac{W}{cm}$

The stress distributions are plotted in Fig. 5.32. A positive value corresponds to a tensile stress in the corresponding direction, whilst a negative value denotes a compressive stress. These stresses will cause refractive index changes, which is called **stress-induced birefringence**. This can change the polarization of the laser mode and thus degrades polarization quality in laser systems. However, these effects can be compensated for by more complex laser designs, in which several laser rods and polarization rotators are used.

The main problem for high average power lasers, however, is the tensile stress on the outer crystal surface. Owing to the perpendicularity of the tangential and axial stress, the total stress on the surface results in

$$\sigma_{tot} = \sqrt{\sigma_t^2 + \sigma_z^2} = 2\sqrt{2}\sigma_0 R_0^2 \tag{5.90}$$

If this tensile stress exceeds a certain value σ_{max}, it will lead to a growth of microscopic cracks on the outer crystal surface, which finally results in a total crystal fracture. Using Eq. (5.78), this maximum stress corresponds to a maximum power dissipation per crystal length of [3]

$$\frac{P_{therm}^{max}}{L} = 8\pi \frac{\lambda_{th}(1-\nu)}{\sqrt{2}\alpha_{th}E}\sigma_{max} = 8\pi R_s, \tag{5.91}$$

which is independent of the rod diameter, where, R_s is the **thermal-shock parameter**, which is shown in Table 5.3 for several laser hosts. This effect yields for YAG, that a thermal extraction of approximately 200 W/cm will fracture the rod. However, this value depends strongly on the surface finish of the laser rod and the real value at which fracture occurs can differ from this value by up to a factor of three.

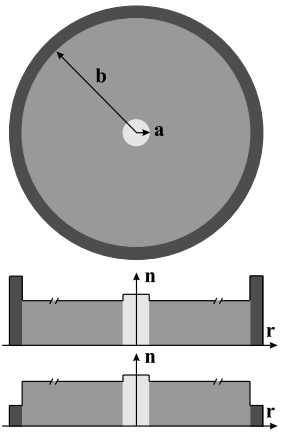

Fig. 5.33 Geometry and refractive index profile of two step-index fibers. The standard fiber only allows core propagation while the double-clad fiber is coated by an outer polymer with lower refractive index than the cladding and thus also allows guiding in the cladding

In order to avoid all these temperature-dependent effects to a great extent, the following laser types have been developed, namely, the fiber laser and the thin-disk laser.

5.3.2 The Fiber Laser

An optical fiber consists of a core with radius a and a refractive index n_{core}, and a cladding with radius b, showing a lower refractive index $n_{cladding} < n_{core}$ as shown in Fig. 5.33. In a fiber laser, this core is in addition doped with laser-active ions, which are pumped by a pump radiation also guided in the fiber.

Owing to the high surface-to-volume ratio

$$\frac{2\pi a L}{\pi a^2 L} = \frac{2}{a} \tag{5.92}$$

and the small fiber radii $a < 1$ mm, the heat transfer from the active core to the large surface occurs over a small distance. Thus, the resulting temperature differences are low, even for the lower thermal conductivities of glass materials. This causes a lower temperature in the active region, and therefore, a higher laser efficiency, especially for quasi-three-level lasers. In a rotationally symmetric fiber a parabolic temperature profile will develop; however, this will only cause a refractive index difference of

$$\Delta n_{therm} \approx \frac{P_{therm}}{4\pi\lambda_{th} L}\frac{\partial n}{\partial T} = 8 \cdot 10^{-6} \tag{5.93}$$

for a $P_{th} = 1$ kW dissipating, $L = 100$ m-long silica fiber ($n \approx 1.45$) with NA $=$ 0.04, $\lambda_{th} \approx 1\ \frac{\mathrm{W}}{\mathrm{K\,m}}$ and $\frac{\partial n}{\partial T} = 10^{-5}\ \mathrm{K}^{-1}$. Comparing this with the refractive-index difference causing the guiding in the fiber, we obtain

$$\Delta n_{guide} \approx \frac{\mathrm{NA}^2_{core}}{2n^2_{core}} = 5 \cdot 10^{-4}. \tag{5.94}$$

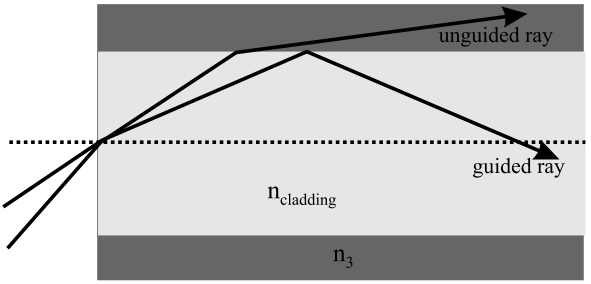

Fig. 5.34 Path of a light ray coupled into the cladding of a fiber

Thus, even for very high thermal power dissipations, the fundamental guiding properties of the fiber stay unchanged, and therefore, the beam quality of the fiber laser will be preserved in the case of a single-mode fiber even for high output powers in the kW range.

Double-Clad Fibers

As a protection the fiber is usually coated by an outer polymer. Its refractive index n_3 therefore determines, whether light may be guided in the cladding or not. As the refractive index profiles consist of several steps, this fiber type is called **step-index fiber**. The cladding diameter is usually much larger than the wavelength, and therefore the propagation within the cladding can be calculated in the scope of geometrical optics. Thus, all light that will hit the fiber end within an acceptance solid angle $\Delta\Omega_0$ with a half angle θ_i will be guided inside the cladding, see Fig. 5.34. This angle can be calculated from the total-internal-reflection angle inside the fiber as

$$\Delta\Omega_0 = 2\pi(1-\cos\theta_i) = 2\pi\left(1-\sqrt{1-\mathrm{NA}_{cladding}{}^2}\right). \tag{5.95}$$

This acceptance cone thus only depends on the numerical aperture of the cladding, given by $\mathrm{NA}_{cladding} = \sqrt{n_{cladding}^2 - n_3^2}$.

In a standard fiber, the polymer usually has a higher refractive index than the cladding, so that no total-internal reflection is possible. This is mostly used for passive fibers, e.g. in telecommunication. In the opposite situation, the cladding can also transport light, and the fiber is called a **double-clad fiber**.

The guiding in the core can be explained in the same way, however, as a result of the smaller core sizes the guiding needs to be calculated by wave optics, which is discussed later. As the guiding core has a higher refractive index than the cladding, the light guided in the cladding can also pass the core of the fiber. This is important for high-power fiber lasers, in which the pump radiation is coupled into the cladding of the fiber, from which it will be absorbed each time it passes the core. The fluorescence is then emitted from the excited ions into the core and the cladding. However,

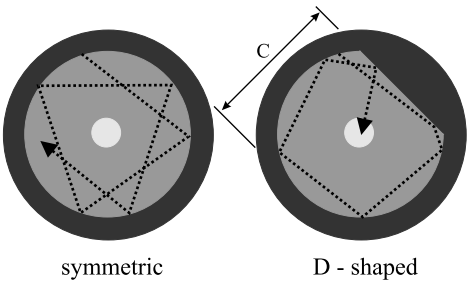

Fig. 5.35 Double-clad fiber with symmetric and D-shaped geometry

only those photons will be amplified to a great extent which only propagate inside the core. Thus, the laser radiation will be guided in the core. Owing to the smaller core size, the laser radiation exhibits a much higher beam quality than the pump radiation. Therefore, the double-clad fiber laser can also be seen as a brightness transformer (or brightness enhancer), transforming the light of the cladding (with a low brightness, a high number of modes and therefore a low beam quality) into the light guided in the core, which shows a high brightness and is emitted into only a few or a single mode, thus having a very high beam quality. Of-course, this is not a true transformer, as the emitted light shows a frequency different from the incoming pump radiation.

However, in double-clad fibers it has to be taken into account that skew waves can build up in completely rotational symmetric index profiles. These skew waves do not pass through the core during their propagation inside the fiber, and therefore, would not be absorbed by the active ions. To obtain a maximum pumping efficiency, these skew waves have to be suppressed, which can be obtained by breaking the rotational symmetry of the fiber. This can be done in several ways, from which the easiest one consists of milling a flat surface on to the fiber preform prior to fiber pulling. This results in the geometry shown in Fig. 5.35. Usually, about 10–15 % of the fiber diameter are cut away ($c \approx 1.8b$), creating a linear reflection edge which breaks the rotational symmetry and makes self-consistent rays that do not hit the core impossible. Assuming a homogeneous filling of the cladding by the pump radiation, which is a direct consequence of the large amount of excited modes in the cladding, the effective pump absorption inside a double-clad fiber can be expressed by

$$\alpha_{eff} = \frac{A_{core}}{A_{cladding}} \alpha_p = \frac{A_{core}}{A_{cladding}} \sigma_a(\lambda_p) N_1. \tag{5.96}$$

Thus, in a double-clad fiber laser, the pump absorption length can be chosen independently from the length of the laser medium within certain limits. As the cladding can be fabricated with a high numerical aperture using a low-index outer polymer, a high numerical aperture of the cladding can be chosen without changing the mode properties of the fiber core. Thus, very high pump powers can be used. In particular, fiber coupled laser diodes can directly pump such a fiber laser without the need for a high-beam-quality pump laser.

Propagation in the Core

The step in the refractive index between core and cladding, together with the diameter of the core, determine how the light propagates in the core. As the core radius a is usually comparable with the wavelength of the laser emission, we have to solve the wave equation, resulting in the existence of modes in a similar way to those in the laser resonators. Here, we use the scalar wave equation in cylindrical coordinates

$$\frac{\partial^2\Psi}{\partial r^2}+\frac{1}{r}\frac{\partial\Psi}{\partial r}+\frac{1}{r^2}\frac{\partial^2\Psi}{\partial\phi^2}+\frac{\partial^2\Psi}{\partial z^2}+n(r)^2k_0^2\Psi=0, \tag{5.97}$$

where, Ψ corresponds to a component of the electric or magnetic field of the light inside the fiber, $n(r)$ is the refractive index and $k_0=\frac{2\pi}{\lambda_s}$ the wave vector of the laser radiation in vacuum. In order to solve this equation, we assume a wave propagating along the fiber axis with a propagation constant β as

$$\Psi(r,\phi,z)=\psi(r)e^{-il\phi}e^{-i\beta z},\quad l=0,\pm1,\pm2,\ldots, \tag{5.98}$$

where, we already took into account that the wavefunction needs to be unambiguous in the azimuthal direction, resulting in an azimuthal mode number l. Using the abbreviations $k_1^2=n_{core}^2k_0^2-\beta^2$ and $k_2^2=\beta^2-n_{cladding}^2k_0^2$, Eq. (5.97) can be transformed into a standard differential equation

$$\frac{\partial^2\psi}{\partial r^2}+\frac{1}{r}\frac{\partial\psi}{\partial r}+\left(k_1^2-\frac{l^2}{r^2}\right)\psi=0,\quad r<a, \tag{5.99}$$

$$\frac{\partial^2\psi}{\partial r^2}+\frac{1}{r}\frac{\partial\psi}{\partial r}+\left(k_2^2+\frac{l^2}{r^2}\right)\psi=0,\quad r>a. \tag{5.100}$$

These are the Bessel differential equations, which are solved by the Bessel functions J_l and K_l

$$\psi(r)\propto J_l(k_1r),\quad r<a \tag{5.101}$$

$$\psi(r)\propto K_l(k_2r),\quad r>a. \tag{5.102}$$

In the case of small refractive index differences $\Delta n=\frac{\mathrm{NA}_{core}^2}{2n_{core}^2}<0.01$, the modes guided by the fiber are linearly polarized [30]. They are therefore called **LP modes**. To describe these modes, the **fiber parameter**, **V parameter**, or **normalized frequency**

$$V=\frac{2\pi a\mathrm{NA}_{core}}{\lambda}, \tag{5.103}$$

is used. Therein, $\mathrm{NA}_{core}=\sqrt{n_{core}^2-n_{cladding}^2}$ is the numerical aperture of the core. The fiber parameter can also be used to express the number of propagating modes M of the fiber, given by

$$M=\frac{4V^2}{\pi^2}+2\quad\text{for } V\gg1. \tag{5.104}$$

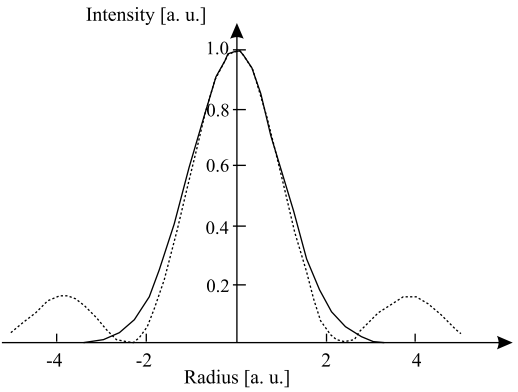

Fig. 5.36 Intensity distribution of a Gaussian and a Bessel function

It can be shown that for $V < 2.405$, i.e. the zero of the lowest Bessel function, only the fundamental mode LP_{01} is guided in the fiber. These fibers are called monomode or single-mode fibers. However, it has to be taken into account that two LP_{01} modes exist which have perpendicular polarizations.

The transverse intensity profile of this fundamental mode LP_{01} is, however, very similar to the one of a Gaussian beam with power P as can be seen in Fig. 5.36, especially for the central lobe which is the one propagating in the fiber. Thus, we can assume a Gaussian distribution in the fiber core given by [48]

$$I(r) = \frac{2P}{\pi w_0^2} e^{-\frac{2r^2}{w_0^2}}, \tag{5.105}$$

for which the mode field radius can be calculated by the empiric formula

$$w_0 = a\left(0.65 + 1.619V^{-1.5} + 2.876V^{-6}\right). \tag{5.106}$$

Spectroscopic Properties of Fiber Lasers

In the following we will discuss the spectroscopic properties of fiber lasers. They differ from the properties of bulk solid-state lasers as a result of the influence of the waveguide effect in the fiber. As an example, we will investigate a Tm^{3+}:ZBLAN fiber laser. Comparing the overlap between absorption and emission in Fig. 5.37, it is evident that a Tm^{3+}-doped ZBLAN fiber laser can be operated as a laser or amplifier in a range between 1.85 µm to over 1.95 µm. Below this range the reabsorption will be too high and one would have to use small fiber lengths and thus small pump volumes. Above this range the gain becomes too low and the intrinsic losses thus result in high laser thresholds and low efficiencies.

In this context, it has to be noted that the emission cross section can only be determined either by measuring the fiber preform or by recording the fluorescence emitted perpendicularly from the outer fiber surface. This arises from the fact that the waveguiding along the fiber axis strongly changes the fluorescence spectrum of

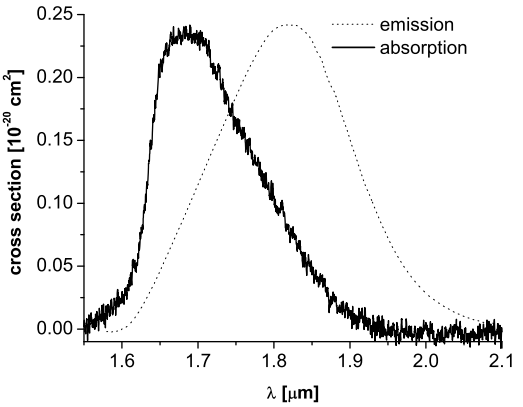

Fig. 5.37 Cross sections of stimulated emission and absorption of Tm^{3+}:ZBLAN [31, 32]

the guided light. To model this, we start from the radiation transport equation of the spectral signal power in a pumped medium

$$\frac{\partial \tilde{P}_s(z)}{\partial z} = \Gamma\big[\sigma_e N_2(z) - \sigma_a N_1(z)\big]\tilde{P}_s(z) + \sigma_e \Gamma \tilde{P}_0 N_2(z), \tag{5.107}$$

wherein N_1 and N_2 are the population densities of the lower and upper laser level, respectively. The mode overlap factor between the guided Gaussian mode and the doped core is given by

$$\Gamma = 1 - e^{-\frac{2a^2}{w_0^2}}. \tag{5.108}$$

Assuming that all ions are either in the ground state or the excited state so that $N_1(z) + N_2(z) = N_g = N_{Tm}$ is the total Tm^{3+}-doping density, we obtain for the amplification of a signal at a wavelength λ_s in a fiber of length L

$$G(\lambda_s) = e^{\int_0^L \Gamma[\sigma_e(\lambda_s)N_2(z') - \sigma_a(\lambda_s)N_1(z')]dz'}. \tag{5.109}$$

We now assume that the maximum amplification of the fiber is G_{max} and occurs at a wavelength λ_{max}, which can be calculated from

$$\frac{\partial G(\lambda_s)}{\partial \lambda_s} = 0. \tag{5.110}$$

The maximum gain wavelength thus solves the equation

$$\frac{\partial \sigma_e(\lambda_s)}{\partial \lambda_s} = \frac{\partial \sigma_a(\lambda_s)}{\partial \lambda_s}\left(\frac{\sigma_e(\lambda_s) + \sigma_a(\lambda_s)}{\frac{\ln G_{max}}{\Gamma N_g L} + \sigma_a(\lambda_s)} - 1\right). \tag{5.111}$$

In this equation, only the spectroscopic properties of the fiber and its length occur. It is therefore independent of the real axial repartition of the ion densities $N_i(z)$. The cross sections are then expressed by a sum of Gaussian functions and a numeric root finding algorithm can be used to obtain λ_{max}.

However, in order to obtain the fluorescence spectrum at the fiber end, we have to integrate the radiation transport equation including spontaneous emission. For

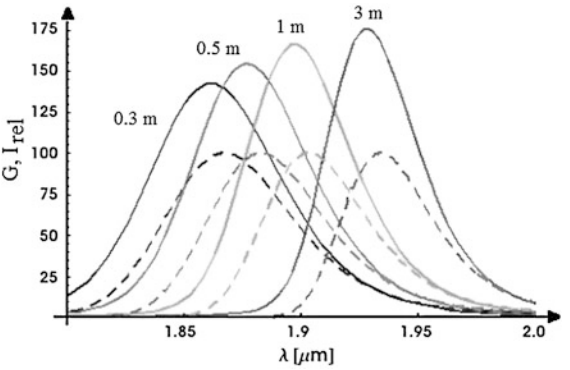

Fig. 5.38 Calculated fluorescence solid line) and gain profile (dashed line) of a Tm^{3+}:ZBLAN fiber. The fiber lengths correspond from left to right to 0.3 m, 0.5 m, 1 m and 3 m, following the maxima in the curves

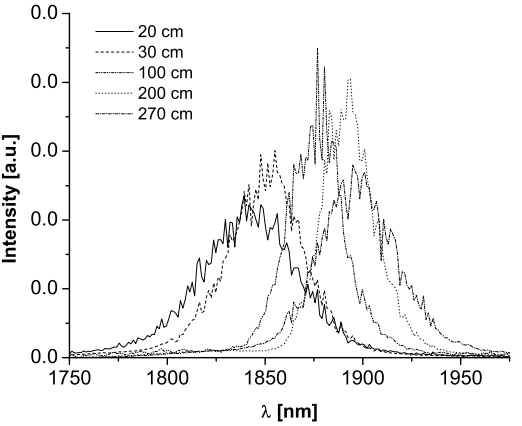

Fig. 5.39 Measured fluorescence of a Tm^{3+}:ZBLAN fiber under excitation at 792–805 nm for different fiber lengths L

simplicity, we assume a homogeneous distribution of the excitation density. This results in a relative fluorescence intensity of

$$I_{rel}(\lambda) = \frac{\sigma_e(\lambda)}{\sigma_e(\lambda) + \sigma_a(\lambda)} \big(G(\lambda) - 1\big)\left(1 + \frac{\sigma_a(\lambda) N_g \Gamma L}{\ln G(\lambda)}\right), \tag{5.112}$$

with

$$G(\lambda) = e^{\frac{\sigma_e(\lambda)+\sigma_a(\lambda)}{\sigma_e(\lambda_{max})+\sigma_a(\lambda_{max})}[\ln G_{max} + \Gamma N_g L \sigma_a(\lambda_{max})] - \Gamma N_g L \sigma_a(\lambda)}. \tag{5.113}$$

This simple relation only holds for axially constant population densities.

The result of the simple calculation is shown for a fiber with $\Gamma = 0.788$ and $N_g = 3.95 \times 10^{26}$ m^{-3} at a maximum amplification of $G_{max} = 100$ in Fig. 5.38. It shows a shift of the maximum of the fluorescence with increasing fiber length and a simultaneous decrease in fluorescence bandwidth. These effects arise from the re-absorption, which increases with increasing fiber length.

The experimental results can be seen in Fig. 5.39 and correspond well to the theory regarding the wavelength shift. However, in this experiment the maximum gain was probably not identical for all fiber lengths, causing the differences in absolute values.

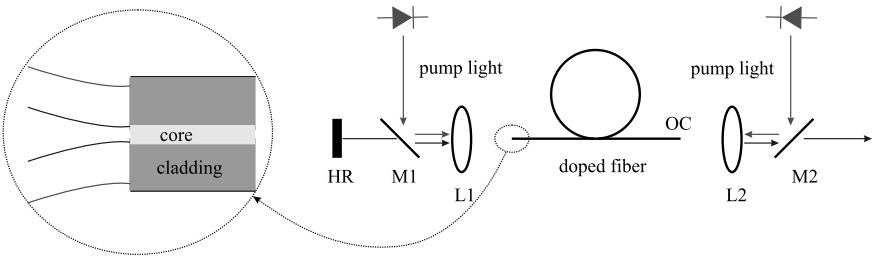

Fig. 5.40 Schematic of the experimental setup of a fiber laser

Experimental Arrangements of Fiber Lasers

The principle experimental arrangement of a double-clad fiber laser can be seen in Fig. 5.40. For a core-pumped fiber laser, this setup only differs in the fact that the pump light needs to have a better beam quality and that the cladding has a lower index of refraction compared with the core. In order to obtain an evenly distributed excitation and heat load, the fiber is usually pumped from both ends. In many laboratory configurations, often free-space resonators are still used to have a maximum number of adjustable parameters in the arrangement and the possibility to include various elements into the cavity. Here, dichroic mirrors (M1 and M2) are used to combine the pump radiation with the laser mode. The pump beams are then launched into the fiber by two lenses (L1 and L2), which simultaneously act as collimation lenses for the laser mode. On one side, the laser beam is retro-reflected by an external highly-reflecting mirror (HR), forming the **external cavity**. Owing to the high gain achieved in the long fiber, a large amount of outcoupling can be used. Therefore, it is often sufficient to simply use the perpendicularly-cleaved fiber end on the other side of the fiber as the OC mirror. This provides a Fresnel reflectivity of

$$R_{OC} = \left(\frac{n-1}{n+1}\right)^2, \tag{5.114}$$

which is around 3.4 % for silica fibers with a refractive index of $n \approx 1.45$. One advantage of this external-cavity design is the free-space propagation of the intracavity beam, which enables the insertion of modulators for Q-switching or of frequency-selective elements such as etalons for wavelength selection and tuning. However, the external-cavity configuration has one drawback, which is the increase in intracavity losses due to the coupling losses that occur when the laser light is re-injected into the fiber core. As this re-injection efficiency strongly depends on the mode matching between the reflected beam from the HR mirror and the guided mode of the fiber, the external cavity has to be well designed and aligned.

In order to avoid this adjustment problem in cw high-power lasers, an all-fiber solution can be produced, as shown in Fig. 5.41. Pump combiners are used to couple the pump light into the cladding. These combiners consist of several smaller

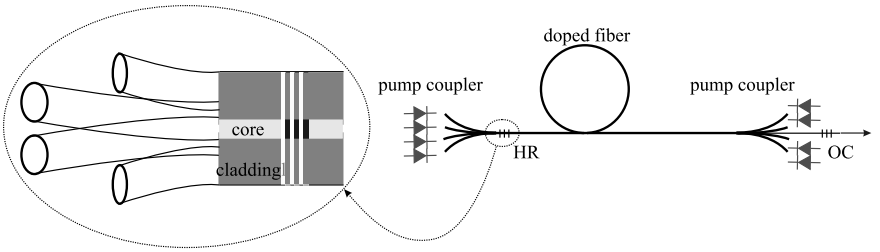

Fig. 5.41 Schematic of the experimental setup of a fiber laser in an all-fiber design without external components

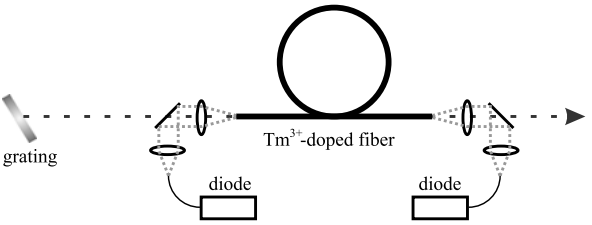

Fig. 5.42 Schematic of the experimental setup of a grating-tuned fiber laser

undoped multi-mode fibers which are **spliced**, i.e. welded, to the cladding of an undoped double-clad fiber that matches the doped laser fiber in diameter and index profile. Thus, the core of this passive fiber is a freely accessible port for the configuration of the cavity, whilst the smaller pump fibers are connected to high-power laser diodes for pumping. Finally, this undoped **combiner** is spliced to the doped laser fiber.

To obtain a fully self-contained, i.e. all-fiber design, fiber laser without any intracavity free-space propagation, **Bragg gratings** are written into both ends of the fiber core to act as HR and OC mirror. These Bragg gratings are a periodic refractive index structure similar to dielectric mirrors. However, they are not created by a thin-film deposit. This refractive index pattern is written into the fiber by illumination of the fiber with a UV-laser-created interference pattern, e.g. by using an Ar^+-ion laser, or by a femtosecond laser. Such Bragg gratings have very sharp resonances with high reflectivity and are written for a specific wavelength. However, slight tuning is possible, e.g. by heating or cooling of the Bragg grating, or by stretching the grating-containing part of the fiber.

Examples of a CW Fiber Laser Based on Tm^{3+}

As an example, Fig. 5.42 shows the experimental arrangement of a Tm^{3+}:ZBLAN fiber laser, which is pumped from both sides by two fiber-coupled laser diodes at 792 nm [2]. The fiber has a core diameter of 30 µm, NA = 0.08, and a cladding diameter of 300 µm, NA = 0.47. In this setup the cavity was built by a retro-reflective mirror (or grating) and the other polished fiber end, i.e. with an OC reflectivity of

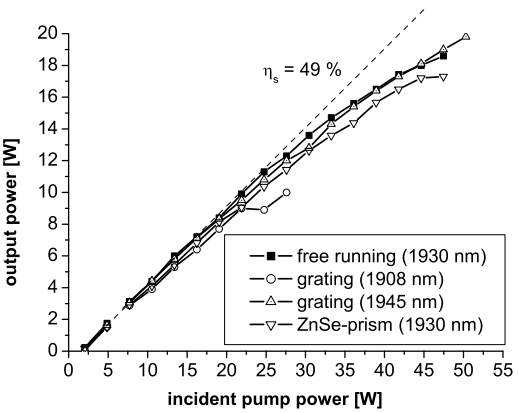

Fig. 5.43 Measured output power of a Tm^{3+}:ZBLAN fiber laser tuned to different wavelengths

$R \sim 4$ %. The emission wavelength was coarsely set by the fiber length and the optimum pump absorption was adjusted by arranging for an appropriate ratio between core and cladding area. The experimental performance can be seen in Fig. 5.43. As expected by the long upper-state lifetime and the negligible multi-phonon relaxation in ZBLAN visible in Table 5.2, the threshold is very low and due to the efficient cross-relaxation mechanism a high slope efficiency of 49 % with respect to the launched pump power is achieved. At high pump powers a **thermal roll-over** occurs, which is not connected to thermal lensing but results from the heating of the fiber, which was uncooled in this arrangement [35].

An interesting effect is the wavelength independence of the laser efficiency over a broad wavelength range, which was also confirmed for different modes of operation of the fiber, used as a fiber laser, an amplifier or as a free-running amplified-spontaneous-emission (ASE) source. The arrangements operated at completely different wavelengths and therefore at different emission cross sections and reabsorption levels as can be seen in Fig. 5.44.

This effect occurs as a result of the amorphous nature of the glass host and shows that an inhomogeneously broadened laser medium can react as quasi-homogeneously broadened. In the glass host the crystal field varies between different positions in the fiber, resulting in a position-dependent Stark-level splitting and energy shift for the Tm^{3+} ions in the fiber. However, these site-to-site shifts in the energy levels correspond approximately to the Stark-splitting within the manifolds. Therefore, a given wavelength within the large emission band can interact with nearly all the Tm^{3+} ions in the fiber, connecting however different levels in each ion. In this way, a given wavelength can extract energy from nearly all of the ions and the medium acts quasi-homogeneously. Only at the lower and upper limit of the emission range is this effect reduced resulting from a lower possibility of transitions that match the wavelength.

This quasi-homogeneous-broadening effect is also found in Tm^{3+}:silica, as can be seen in Fig. 5.45. A Tm^{3+}-doped silica fiber with a core diameter of 20 µm, NA = 0.2, and a cladding diameter of 300 µm, NA = 0.4 has been used. The optimum fiber length was found to $L = 2.3$ m from the measurements also shown in Fig. 5.45.

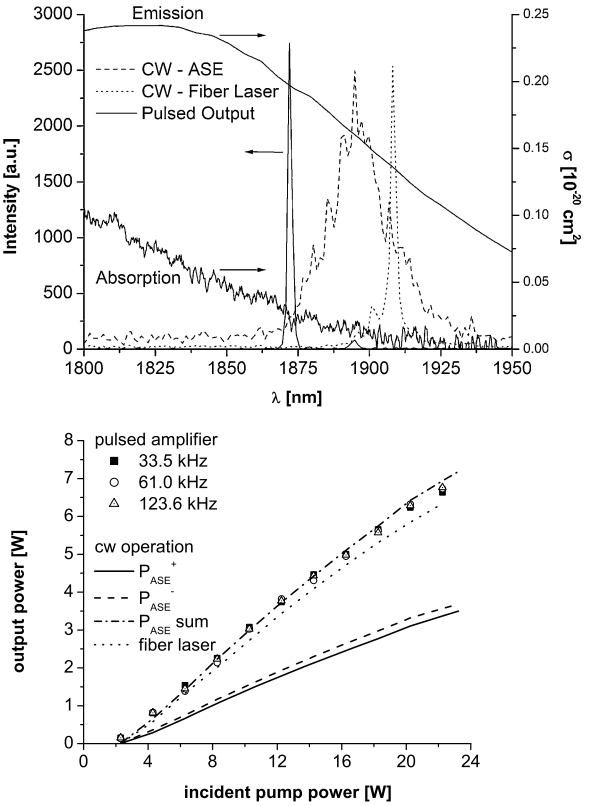

Fig. 5.44 Measured output spectra and output powers of a Tm^{3+}:ZBLAN fiber in different operation types. The total sum of the emitted powers at both fiber ends in the case of an operation as an ASE source, the output power as a fiber laser and as an amplifier is comparable [41]

Q-Switched Fiber Lasers

In contrast to low repetition rate Q-switched operation of, e.g. a Tm^{3+}:YAG laser [33], in which the maximum laser efficiency is determined by the ratio between the pump pulse duration and excited state lifetime given by Eq. (4.6), high-repetition rate ($\nu_{Rep} \gg \frac{1}{\tau}$) Q-switched Tm^{3+} fiber lasers can be as efficient as in cw operation [2, 34, 36, 37]. In Tm^{3+}:ZBLAN, owing to its long upper level lifetime, a low intracavity laser intensity is sufficient to saturate the laser transition. Thus single-pass amplifiers can be easily realized, reaching the same efficiency as in continuous-wave laser operation [38–42]. However, as a result of the very high laser signal saturation intensity in Tm^{3+}:silica, cavity losses, as for example the re-injection efficiency in an external cavity, need to be minimized to get highly efficient operation [2].

Especially for pumping applications, in which Q-switched fiber lasers are e.g. used to pump non-linear converters, and where high average output powers are needed, the high repetition rate fiber lasers lead to stable and compact system architectures. As a result of the guiding effect in fibers, a strong influence of amplified spontaneous emission (ASE) on the laser properties exists, and it can be shown that ASE becomes a non-negligible effect when the amplification along the fiber exceeds

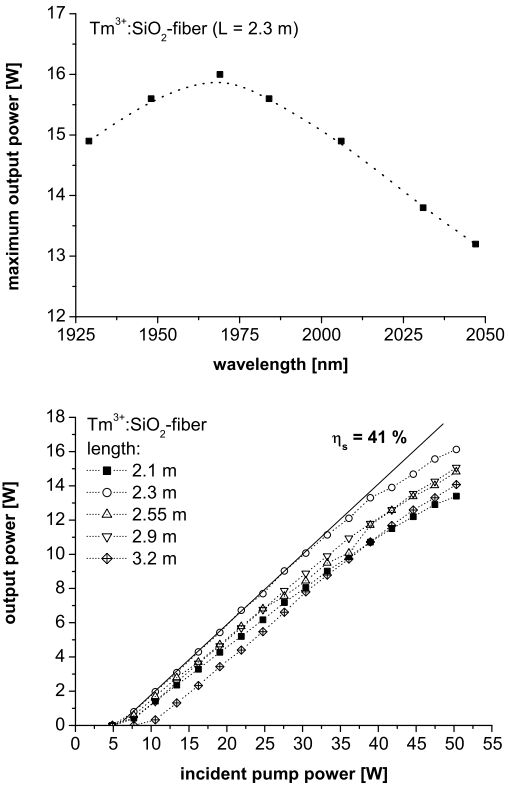

Fig. 5.45 Measured output power of a Tm^{3+}:silica fiber laser versus wavelength and fiber length

a factor of 100, i.e. 20 dB. However, as recent investigations on a Tm^{3+}:silica fiber laser have shown, ASE effects can be efficiently avoided in Q-switched fiber lasers at high repetition rates through good design [36]. The experimental arrangement is shown schematically in Fig. 5.46. An AOM is inserted into the external cavity for Q-switching and a telescope increases the beam diameter on the end mirror, where there is a diffraction grating for wavelength tuning, to avoid optical damage at high pulse energies. Also EOM cavity blocking can be used; however, as this fiber is not polarization maintaining, an AOM provides much lower insertion losses than an EOM and a polarizer.

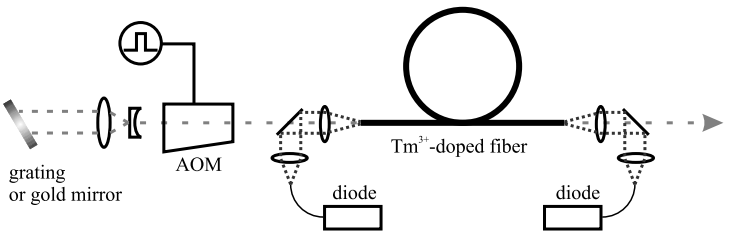

Fig. 5.46 Schematic of the experimental setup of an acousto-optically Q-switched fiber laser

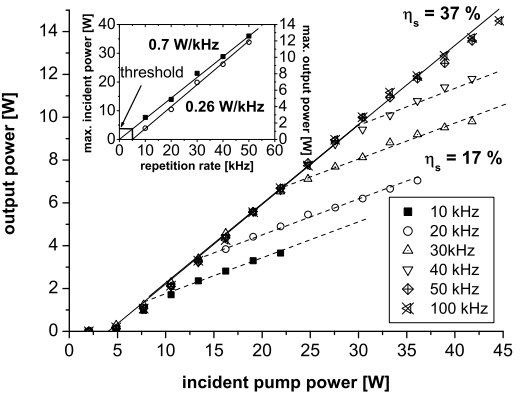

Fig. 5.47 Average output power of a Q-switched Tm^{3+}:silica fiber laser at different repetition rates as a function of the incident pump power [36]. The inset shown the dependence of the maximum allowable pump power and the corresponding output power as a function of the repetition rate

The results are shown in Fig. 5.47. A deviation of the output power from the 37 % slope line of the CW laser is observed. This deviation is repetition rate dependent and the direct result of ASE buildup at high pump intensities. These high pump powers lead to an inversion reaching a value for which the intracavity modulator could not generate enough losses in order to suppress ASE before the next pulse is released. Therefore a further increase in output power is only connected to the half of the original slope efficiency as the ASE is emitted from the fiber in both directions. It could be shown that this point of deviation in output power is linearly linked to the repetition rate, an effect that will be explained in the following discussion.

Using the Q-switch theory presented in Sect. 4.1.1 for a repetitively Q-switched laser, the initial inversion increases with pump power and is limited by the maximum population inversion $\langle \Delta N \rangle_\infty$, which would be reached at the incident pump intensity $I_{p,0}$ in the blocked cavity without a laser signal present for $t \to \infty$, given by

$$\langle \Delta N \rangle_\infty = \frac{2\lambda_p \tau}{hc} \frac{\eta_{abs}}{L} I_{p,0} - \langle N \rangle. \tag{5.115}$$

However, even in the blocked cavity $\langle \Delta N \rangle_\infty$ will never be reached as the buildup of ASE will limit the inversion to a lower value $\langle \Delta N \rangle_\infty^{ASE}$, which corresponds to the ASE threshold $I_{p,0}^{ASE}$ of the fiber. This pump intensity at which ASE dominates the fiber dynamics can even be reduced due to residual feedback caused by imperfect cavity blocking, for example as a result of the OC fresnel reflection of the fiber output end.

Owing to the upper limit in $\langle \Delta N \rangle_i$ given by $\langle \Delta N \rangle_\infty^{ASE}$, a maximum pulse energy can be generated in a given fiber arrangement, which depends on cavity blocking and fiber parameters. Using Eq. (4.28), which can be rewritten as

$$\frac{\langle \Delta N \rangle_f'}{\langle \Delta N \rangle_i'} = e^{-r\eta_e(r)}, \tag{5.116}$$

in which r is the ratio between pump and threshold power and $\eta_e(r)$ the extraction efficiency, and Eq. (4.57), the initial population inversion in repetitive Q-switched operation can be written as

$$\langle \Delta N \rangle_i' = \langle \Delta N \rangle_\infty' \frac{1 - e^{-\frac{1}{\tau \nu_{Rep}}}}{1 - e^{-r\eta(r)} e^{-\frac{1}{\tau \nu_{Rep}}}}, \tag{5.117}$$

which simplifies to

$$\langle \Delta N \rangle_i' = \langle \Delta N \rangle_\infty' \left(1 - e^{-\frac{1}{\tau \nu_{Rep}}}\right) \tag{5.118}$$

for $r \gg 1$, see Fig. 4.6. At high repetition rates $\nu_{Rep} \gg \frac{1}{\tau}$, this expression can be approximated and yields

$$\langle \Delta N \rangle_i' \approx \frac{\langle \Delta N \rangle_\infty'}{\tau \nu_{Rep}} \propto \frac{P_{p,0}}{\tau \nu_{Rep}} \tag{5.119}$$

in the case of low ground-state depletion. Owing to the upper limit in $\langle \Delta N \rangle_i$ given by $\langle \Delta N \rangle_\infty^{ASE}$, the point of deviation from linearity corresponds to a linear relation between the maximum allowable pump power $P_{p,0}^{max}$ and the repetition rate,

$$P_{p,0}^{max} = k_p \nu_{Rep}. \tag{5.120}$$

The linear slope relation between pump and output power then causes a corresponding relation between the laser output power and the repetition rate, given by a factor k_s that can be derived as

$$k_s = \frac{\partial P_{out}(P_{p,0}^{max})}{\partial \nu_{Rep}} = k_p \eta_s, \tag{5.121}$$

where, η_s is the laser slope efficiency. These theoretical predictions well agree with the experiment as can be seen in Fig. 5.47. The corresponding proportionality factors found were $k_p = 0.7\ \frac{\mathrm{W}}{\mathrm{kHz}}$ and $k_s = 0.26\ \frac{\mathrm{W}}{\mathrm{kHz}}$ for incident pump powers up to 45 W. This shows that under high-repetition-rate operation, high average powers can be achieved with Q-switched fiber lasers.

To maximize the generated pulse energy a careful laser design is needed to increase the ASE threshold of the blocked cavity, allowing high pump powers above laser threshold, i.e. high values of r, which then result in very short pulses according to Eq. (4.30) and Fig. 4.6. This was also verified experimentally, where short pulses of 41 ns could be achieved from a 2.3 m long Tm^{3+}-doped silica fiber at $r = 15$ [36]. As a comparison, Q-switch theory results in a pulse width of 30 ns for this fiber, taking into account a cavity round-trip time of $\tau_{RT} \approx 22$ ns, which can be seen as the cavity photon lifetime resulting from the strong outcoupling. This shows that in order to obtain short pulses and to push the ASE threshold as high as possible, a very low OC reflectivity has to be used in Q-switched fiber lasers.

Power Limits in Fiber Lasers

The fact that the laser mode is concentrated in the small core in a fiber laser causes three different constraints in output power, depending on the spectral and temporal

properties of the laser radiation. The first limit is connected to the finite optical-damage threshold of silica glass, which is on the order of 3 GW/cm^2. This is the intensity, at which a damage is created on the surface of the glass, usually together with the formation of a plasma and the vaporization of parts of the glass surface. For the example of a 30 µm-diameter core, NA = 0.04 fiber at a wavelength around 1 µm, a mode field radius of $w_0 = 13$ µm is calculated from Eq. (5.106) and results in a damage threshold of

$$P_{max} = \frac{\pi w_0^2}{2} \hat{I} = 8 \text{ kW}. \tag{5.122}$$

At this power, damage to the fiber end faces can occur, making it necessary to re-cleave or to repolish the fiber ends. It is important to note that this limit gives an instantaneous power, i.e. it is independent of the temporal mode of operation of the fiber laser and has the same value for a cw fiber laser, where it denotes the laser power, and for a pulsed Q-switched fiber laser, where it denotes the maximum pulse peak power at which damage is likely to occur.

The two other processes limiting the output power of a fiber laser are Brillouin and Raman scattering, two intensity-dependent non-linear processes.

Brillouin scattering In Brillouin scattering, a photon of the laser field propagating in the fiber is scattered by an acoustic phonon. Consequently, the most efficient scattering occurs with longitudinal acoustic phonons. Is a phonon created during that process, the laser photon gets red-shifted by an amount of ν_B, which is a function of the fiber material and the scattering angle between the photon and the phonon. This is called the **Stokes process**. In the reverse case, i.e. when a phonon is annihilated in the scattering process, the photon gets blue-shifted, which is called the anti-Stokes process. The maximum frequency shift is obtained in reverse scattering, in which the scattered photon propagates in the opposite direction than the incoming unscattered photon. This maximum frequency shift is given by [43]

$$\nu_B = \frac{2n v_s}{\lambda_0}, \tag{5.123}$$

where, v_s denotes the velocity of sound of the longitudinal phonons, n the refractive index of the host medium and λ_0 the wavelength of the incoming, unscattered radiation, the so-called **Brillouin pump radiation**. For ZBLAN this results in $\nu_B \approx 18.82$ GHz [45].

The interference between the back-scattered light and the incident pump radiation creates an intensity pattern. When the spatial period of this pattern corresponds to the phonon wavelength and propagates itself with the velocity of sound in the medium, the lattice deformation created by the phonon will be amplified by **electrostriction**. This feedback increases the Brillouin-scattering rate and is called **stimulated Brillouin scattering** (**SBS**). Thus, a threshold exists and for powers above a strong conversion from the incoming radiation into the scattered radiation occurs. However, Brillouin scattering can only occur if the optical pulse width is longer than the average photon lifetime of the medium, which is $\tau_{ph} = 3.3$ ns for the case of ZBLAN.

Table 5.4 SBS thresholds in ZBLAN at 1.87 µm. The real thresholds are calculated for a 0.23 nm-wide signal line.

	Fiber 1	Fiber 2	Fiber 3
L	0.3 m	1.5 m	2.4 m
w_0	3.70 µm	7.2 µm	12.8 µm
$P_{SBS,0}$	602 W	456 W	900 W
P_{SBS}	107 kW	81.2 kW	160 kW

In order to derive an expression for the Brillouin threshold, the Brillouin amplification of a small-line-width pump radiation $\Delta\nu \ll \Delta\nu_B$ is used, given by

$$g_B = \frac{2\pi n^7 p_{12}^2}{\Delta\nu_B c\lambda^2 \rho v_s}, \tag{5.124}$$

where, $\Delta\nu_B = \frac{1}{\pi\tau_{ph}}$ is the Brillouin line width caused by the natural phonon lifetime (natural line width), ρ the density of the fiber medium and p_{12} its elasto-optic coefficient. The frequency-dependent small-signal gain of the SBS shows a Lorentzian line shape and can be described by

$$g_{SBS}(\nu) = g_B \frac{\frac{\Delta\nu_B^2}{4}}{(\nu - \frac{c}{\lambda_0} + \nu_B)^2 + \frac{\Delta\nu_B^2}{4}}, \tag{5.125}$$

and the SBS threshold power for a low line width pump radiation results in [43]

$$P_{SBS,0} \simeq 21 \frac{A_{eff}}{g_B L_{eff}}, \tag{5.126}$$

where, the effective fiber length

$$L_{eff} = \frac{1}{\alpha}\left(1 - e^{-\alpha L}\right) \tag{5.127}$$

is nearly equal to the geometrical fiber length L owing to the low intrinsic losses α in the glass medium. The effective mode area is given by $A_{eff} = \frac{\pi w_0^2}{2}$ and can be approximated in multi-mode fibers by the core area $A = \pi a^2$.

However, if the line width of the laser radiation is much larger than the Brillouin line width of the glass, e.g. $\Delta\nu_B = 96$ MHz in ZBLAN, the Brillouin line width $\Delta\nu_B$ in Eq. (5.124) has to be replaced by the laser line width $\Delta\nu$ [44], resulting in a real Brillouin threshold of

$$P_{SBS} \simeq 21 \frac{A_{eff}}{g_B L_{eff}} \frac{\Delta\nu}{\Delta\nu_B}. \tag{5.128}$$

An example for SBS thresholds is given in Table 5.4. It can be seen, that in contrast to the low thresholds obtained for a small laser line width, a fiber laser or amplifier operating at a line width on the order of 0.1–1 nm shows Brillouin thresholds that are much higher than the optical damage threshold of a standard fiber for short fiber lengths. However, for long fibers the Brillouin threshold can be

much lower than the optical damage threshold and has to taken into account in high power laser systems.

Raman scattering In analogy to Brillouin scattering a photon can also scatter on optical phonons, which is called **Raman scattering**. The Raman effect, however, is different from the Brillouin effect in several points. First, the frequency shifts are much larger owing to the higher phonon energies of optical phonons, causing a frequency shift ν_R in the range of some THz, where the red-shifted radiation is also called the **Stokes radiation**. And second, the decay times of the optical phonons are much shorter than those of the acoustic phonons, causing Raman scatting also to occur at laser pulse widths smaller than 1 ns.

In **stimulated Raman scattering** (**SRS**) a scattering in the same propagation direction as well as in the reverse direction is possible. However, here the lowest threshold is obtained for scattering into the same direction of propagation, resulting in

$$P_{SRS} \simeq 16 \frac{A_{eff}}{g_R L_{eff}}. \tag{5.129}$$

The threshold for reverse scattering is about 25 % higher [43], and thus does not need to be taken into account here. By passing this threshold, a large amount of the incident radiation becomes red-shifted with a high efficiency. In principle, this process can repeat itself for the created Stokes radiation, causing successive Stokes orders exciting the fiber.

The Raman amplification is given by

$$g_R = \frac{4\pi \chi_R''}{\lambda_{st} n^2 \epsilon_0 c}, \tag{5.130}$$

wherein χ_R'' denotes the non-linear susceptibility of the glass medium, and λ_{st} the wavelength of the Stokes-shifted light. In glasses, depending on the chemical composition of the glass, several maxima can occur in the density of states of the phonons, e.g. for ZBLAN one obtains 17.7 THz (590 cm^{-1}), 14.4 THz (480 cm^{-1}), 11.7 THz (390 cm^{-1}), 9.9 THz (330 cm^{-1}), 8.1 THz (270 cm^{-1}) and 6.0 THz (200 cm^{-1}) [46]. The strongest Raman amplification occurs on the 590 cm^{-1} line. In ZBLAN, for example, the Raman gain is about 21 THz wide. Thus, the Raman pump signal, i.e. the laser radiation, can be seen as quasi-monochromatic compared to this large Raman line width, and the threshold does not need to be scaled as we did for the Brillouin scattering.

As an example, Table 5.5 shows the corresponding SRS thresholds for the three fibers of Table 5.4.They are much closer to the optical-damage limit and usually determine the upper laser power limit for long fibers, especially in pulsed operation.

The only possibility to avoid these non-linear effects is the reduction of the laser intensity in the fiber by increasing the mode-field diameter. However, in order not to loose the modal properties of the fiber, the fiber parameter in Eq. (5.103) has to stay constant. As the numerical aperture of a step-index fiber usually has a lower limit of NA ≥ 0.04 as a result of the fiber-manufacturing process, the core diameter

Table 5.5 SRS thresholds for three ZBLAN fibers at 1.87 μm.

	Fiber 1	Fiber 2	Fiber 3
L	0.3 m	1.5 m	2.4 m
w_0	3.70 μm	7.2 μm	12.8 μm
P_{SRS}	26.4 kW	20.0 kW	39.5 kW

is limited to ∼30 μm. Even if lower numerical apertures would be possible, high bending losses would result and the fiber laser would loose its beneficial property of being coiled to obtain a small laser volume. These upper limits in core size are related to the principle of the step-index fiber. Using **photonic-crystal fibers** the effective core diameter can be greatly increased. The guiding in these fibers is not caused by a step in the refractive index, but by a wave-optical effect: The core is surrounded by an air-filled hole pattern, which results in a band-structure for the light frequencies, comparable with the energy band-structure of electrons in a crystalline solid. Thus, for certain wavelength bands, a band-gap exists, and these wavelengths are not allowed to propagate in the structure around the core. This confines the light to the core area. Another simple argument to explain this guiding effect is that by introducing the air holes, the average refractive index of the cladding is lower than the core. However, this simple argument does not allow to explain the frequency-spectrum of the guiding band gaps. These photonic-crystal fibers allow single-mode operation with core diameters of over 100 μm. However, a large core diameter with single-mode guiding corresponds to a small NA fiber. Thus, very high bending losses occur and these fibers have to be aligned straight in order to avoid these losses.

Using these photonic-crystal fibers, single-mode CW output powers of several kW have been realized with Yb^{3+}-doped silica fibers.

Applications

Most high power fiber lasers are Yb^{3+}-doped silica fibers emitting in the 1.03–1.08 μm range and are used in welding and cutting applications. In 2006, the state-of-the-art was 2 kW in a single-transverse mode realized by *IPG Photonics, Burbach, Germany*, while multi-mode fiber lasers generate >10 kW out of a 100–300 μm-core multimode fiber. These systems reach efficiencies of up to 25 %. However, the fiber laser units usually consist of several modules emitting some 100 W, which are then all coupled into a single 100–300 μm-core undoped transport fiber. Due to the low beam quality of the multimode output fiber, these sources can only be used with short distances between the fiber output optics and the workpiece. In 2012, single-transverse-mode fiber lasers of 10 kW output power have been produced—a value close to the damage threshold calculated above. Other important applications are in medicine and arise from the easy delivery of the laser radiation with the fiber, that can be introduced into endoscopes for low-invasive surgery. In these applications, however, a radiation around 2 μm is better suited due to its strong absorption in water.

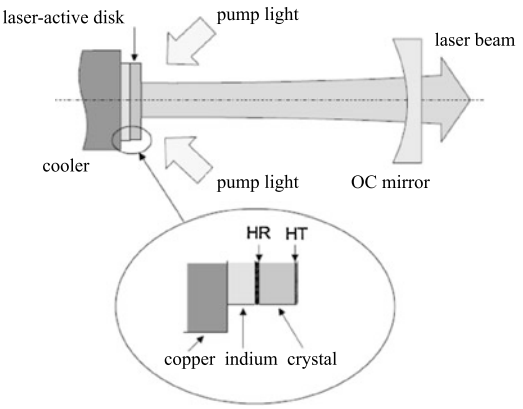

Fig. 5.48 Schematic of a thin-disk-laser setup, showing the laser disk, which is soldered to the heat sink on its HR side using indium solder, and the external OC mirror [47]

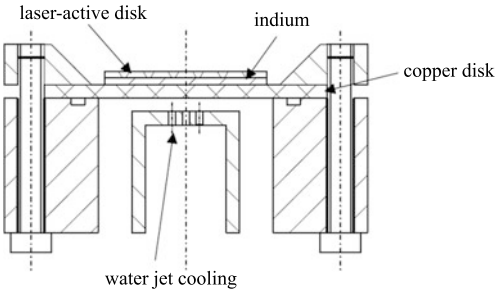

Fig. 5.49 Mechanical design of the disk heat sink with water-jet cooling [47]

5.3.3 The Thin-Disk Laser

The basic idea behind the thin-disk laser is an axial, one-dimensional heat flow within the laser medium towards the heat sink. Therefore, at any axial point along the laser medium, a homogeneous radial temperature distribution is predicted to occur and consequently, no thermal lensing results. The schematic of such a laser is depicted in Fig. 5.48. The laser-active medium is a disk with a diameter of several mm to some cm, with a thickness of some 100 μm. The disk is AR coated for a high transmission at its front face, and HR coated at its back face, with which it is soldered to the copper heat sink using indium or gold solder. The laser cavity is formed by the HR coating on the disk and an external OC mirror. This mirror allows control of the cavity mode size to match the pumped area in the disk.

The heat-sink assembly of the disk is shown in Fig. 5.49. The laser-active disk is soldered with indium on to a larger copper disk, which itself is mounted on to a hollow copper block. Inside this block, a water jet is emitted that hits the back surface of the copper disk for efficient cooling. Water-jet cooling is chosen as it is much more efficient than a simple laminar flow along the copper surface.

The pumping scheme of a disk laser differs from usual longitudinal pumping, as the disk itself shows a small single-pass absorption as a result of the low thickness of the disk. In order to enhance the pump absorption, the pump beam makes multiple passes through the disk. This multi-pass pumping scheme is shown in Fig. 5.50.

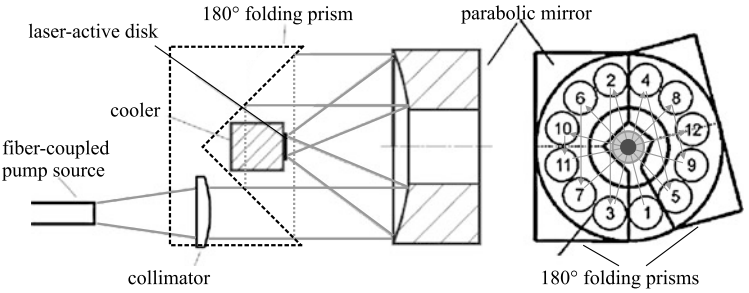

Fig. 5.50 Schematic of the pump system of a disk laser, using a parabolic mirror and retro-reflecting prisms to achieve a total 24-pass ($m = 12$) propagation of the pump radiation [47]

The pump light, usually emitted by a highly-multi-mode fiber or a glass-rod homogenizer, is collimated by a first lens and directed on to a parabolic mirror, which images the fiber output on to the disk. The non-absorbed pump power then is reflected from the disk, hits the parabolic mirror on the opposite radial point and is collimated again. Around the disk-heat-sink assembly, two 180° retro-reflecting prisms are used to flip the residual pump beam propagation path and to direct it on to another spot on the parabolic mirror to perform a second pass through the disk. After being re-collimated by the parabolic mirror, the residual pump light after the second pass hits the other 180° retro-reflecting prism, which is tilted with respect to the first prism. This optical configuration causes the pump beam to make multiple passes through the disk. The optical path lengths in this pump arrangement are chosen so that the disk is imaged on to itself after each pump pass (**relay imaging**).

The theoretical number of passes only depends on the tilt angle between the two prisms. After the first m passes, where m denotes the number of passes through one disk thickness L, the beam hits one of the prisms symmetrically on the reflection axis, causing the beam to be retro-reflected. Therefore, this multi-pass pump optic achieves in total $2m$ pump passes through the disk. The corresponding tilt angle between the two prisms is thus

$$\gamma = \frac{360°}{2m}, \tag{5.131}$$

i.e. 15° for the $2m = 24$ pass setup shown in Fig. 5.50.

The effective number of pump passes through the disk, however, depends strongly on the pump absorption of the disk and the values of the reflectivity of the mirror, prism and disk coatings and the transmission of the AR coating on the disk. Assuming a single-pass disk transmission of

$$T_D = e^{-\alpha_p L}, \tag{5.132}$$

with α_p being the pump absorption coefficient and L the disk thickness, we obtain a residual power after an even number of m passes, i.e. after a number of $\frac{m}{2}$ back- and forth passes (reflections) through the disk, of

$$P_{res,m} = \left(R_P^2 R_{PR}\right)^{\frac{m}{2}-1} \left(T_{HT}^2 R_{HR} T_D\right)^m R_P P_{inc}, \tag{5.133}$$

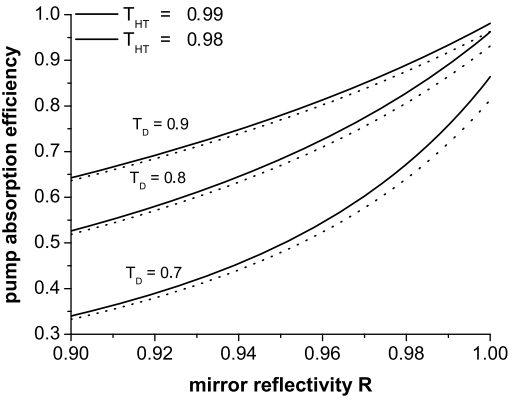

Fig. 5.51 Pump absorption efficiency of a disk laser with a total 24-pass ($m = 12$) propagation of the pump radiation for various single-pass disk transmissions and HT coatings

where, P_{inc} is the incident pump power entering the disk-laser module, R_P the reflectivity of the parabolic mirror, T_{HT} the transmission of the anti-reflection coating on the disk, R_{HR} the reflectivity of the HR coating on the disk for the pump light and R_{PR} the total reflectivity of a prism for one 180° turn. Thus, after the full $2m$ passes the residual pump power is given by

$$P_{res,2m} = \left(R_P^2 R_{PR}\right)^{m-1} \left(T_{HT}^2 R_{HR} T_D\right)^{2m} R_P P_{inc}. \tag{5.134}$$

In analogy, the amount of pump power absorbed during the $\frac{m}{2}$th reflection on the disk is given for an even m by

$$P_{abs,m} = (1 - T_D)(1 + T_D R_{HR}) \left(R_P^2 R_{PR}\right)^{\frac{m}{2}-1} \left(T_{HT}^2 R_{HR} T_D^2\right)^{\frac{m}{2}-1} R_P P_{inc}. \tag{5.135}$$

Summing up all the contributions from the different passes, we obtain the total absorbed pump power as

$$P_{abs,2m}^{tot} = \sum_{k=1}^{m} P_{abs,2k}, \tag{5.136}$$

resulting in

$$P_{abs,2m}^{tot} = R_P (1 - T_D)(1 + T_D R_{HR}) \frac{1 - (R_{HR} R_P^2 R_{PR} T_D^2 T_{HT}^2)^m}{1 - R_{HR} R_P^2 R_{PR} T_D^2 T_{HT}^2} P_{inc}. \tag{5.137}$$

In order to see the effect of the different reflectivities and transmission values on the total pump absorption, we assume a constant reflectivity value for all the different reflective surfaces of $R_{HR} = R_P = R_{PR} = R$. This results in a pump absorption efficiency of

$$\eta_{abs,2m}^{tot} = R(1 - T_D)(1 + T_D R) \frac{1 - (R^4 T_D^2 T_{HT}^2)^m}{1 - R^4 T_D^2 T_{HT}^2}, \tag{5.138}$$

which is shown for different values of T_D and T_{HT} for the case $m = 12$ in Fig. 5.51. It can be seen that for an efficient pump absorption, very good, highly-reflective, mirror coatings are necessary, and a very good anti-reflection coating on the disk

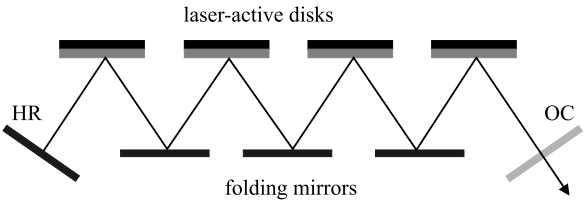

Fig. 5.52 Schematic of a multi-disk setup with a single cavity, in which the total single-pass gain is increased

has to be used. These coatings are especially critical as they have to provide this performance at all the different incident angles occurring for the pump beams, taking into account that the pump light is usually unpolarized after the homogenization in the fiber or glass rod.

Another important point arises from the low gain resulting from the low thickness of the disk. Therefore, a high OC reflectivity has to be used and the intracavity losses have to be minimized to very low values in order to obtain a high laser efficiency. To increase the single-pass gain, several discs can be arranged within one laser cavity as shown in Fig. 5.52. This cavity consists of an OC and a HR mirror at the ends, and a zig-zag path between the different discs using passive folding mirrors. Using this multi-disk design, Yb^{3+}:YAG thin-disk lasers with output powers of >10 kW have been realized for welding and cutting applications in industry.

Power Limitation in Disk Lasers

A main limitation of the performance of disk lasers is the maximum extractable power per disk. This is a function of the disk size and is limited by amplified-spontaneous emission (ASE) mainly occurring in the transverse direction in the disk, where the gain-length product is much larger than in the axial resonator-mode direction. This aspect is especially important for closed paths within the disk, for which at each intersection with the disk boundary a total-internal reflection occurs, the round-trip losses on the path can become very low, resulting in a self oscillation of the disk on the internally trapped modes, called **parasitic modes**. At high OC transmissions, which are used in high-power lasers, these modes may therefore reach their threshold at a pump power much lower than the threshold of the cavity modes. Especially for power scaling, in which in principle an increase of the disk diameter at constant pump intensity should yield very high output powers, the onset of parasitic lasing can set an upper limit on the disk size and output performance of the laser. In a circular disk laser, three different parasitic modes can occur, depending on their main propagation schemes: ring modes, transverse modes and radial modes.

The ring modes are oscillations that are only reflected on the cylindrical outer surface of the disk. Assuming that an efficient reflection will only occur at incident angles θ_r on that surface, which are larger than the critical angle of total-internal reflection

$$\theta_c = \arcsin \frac{1}{n} \tag{5.139}$$

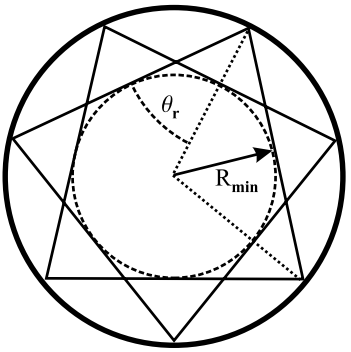

Fig. 5.53 Sketch of a parasitic ASE ring mode reflected on the cylindrical outer surface of the disk

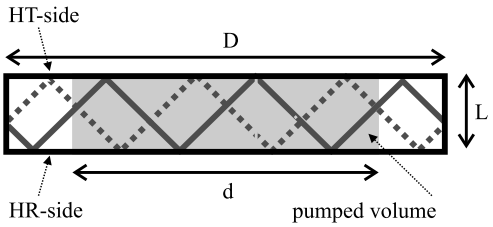

Fig. 5.54 Transverse mode propagation through the disk center

in the laser medium, we directly obtain from Fig. 5.53 that these modes cannot pass an inner disk region with a radius R_{min} given by

$$R_{min} = \frac{D}{2} \sin\theta_c = \frac{D}{2n}, \tag{5.140}$$

where, D is the diameter of the disk and n its refractive index. This relation, is therefore, the key to the suppression of the ring modes in a disk laser. The radius of the pumped area just needs to be smaller than the minimum ring-mode distance from the disk center, given by R_{min}, and possible ring modes do not exhibit a gain during their propagation. In the case of a quasi-three-level laser medium like Yb^{3+}-doped crystals, the strong reabsorption on the laser line in the unpumped part creates an additional loss, helping to suppress the ring modes further. Also, a hybrid disk can be used, in which the outer part is doped with a strongly absorbing ion.

The transverse modes are reflected on the front and back surface of the disk and on the cylindrical part. The maximum gain per mode round trip is obtained for the transverse mode, which propagates through the disk center, shown in Fig. 5.54. Accounting for the angle-dependent reflectivities of the three disk surfaces, this mode should start oscillating when the gain along the propagation path compensates for the reflection losses, i.e. when

$$R_{HR}^k(\theta_a) R_{HT}^k(\theta_a) R_C(\theta_a) e^{\frac{gD}{\sin\theta_a}} = 1, \tag{5.141}$$

where, $R_{HR}(\theta_a)$, $R_{HT}(\theta_a)$ and $R_C(\theta_a)$ are the angle-dependent reflectivities of the HR, HT and cylindrical side of the disk, and k is the number of reflections, given by

$$k = \frac{D}{2L \tan\theta_a}. \tag{5.142}$$

Taking into account that the gain-diameter product gD in Eq. (5.141) accounts for the average gain of the mode propagating from one side to the other, and assuming that only an inner diameter d of the disk is pumped to suppress the ring modes, this average gain-diameter product can be expressed by

$$gD = g_m d - \alpha(D - d), \tag{5.143}$$

where, $g_m = \sigma_e(\lambda_m)N_2 - \sigma_a(\lambda_m)N_1$ is the gain coefficient at the mode's wavelength λ_m inside the pumped volume, assuming homogeneous populations densities within the disk, and $\alpha = \sigma_a(\lambda_m)N_1$ the absorption coefficient of this wavelength in the unpumped part of the disk.

As any kind of optical coating cannot change the total-internal reflection property of an optical medium with respect to its surrounding refractive index, the transverse modes will only be efficiently reflected at the HT side for $\theta_a > \theta_c$. Thus a simultaneous total-internal reflection on the cylindrical surface can only occur at angles of

$$\theta_c < \theta_a < 90° - \theta_c. \tag{5.144}$$

For YAG, this results in $33.3° < \theta_a < 56.7°$. If we now assume that all the reflections are perfect, it follows directly from Eq. (5.143) and Eq. (5.141), that in a four-level-laser medium ($\alpha = 0$) the parasitic modes will immediately oscillate as $g_m d \geq 0$, and no laser action will occur through the cavity modes. For a quasi-three-level laser medium ($\alpha > 0$), we can rewrite the parasitic mode threshold $gD \geq 0$ using $N_1 + N_2 = N_{tot}$ as

$$\frac{N_2}{N_{tot}} \geq \frac{\sigma_a(\lambda_m)}{\sigma_e(\lambda_m) + \sigma_a(\lambda_m)} + \left(\frac{D}{d} - 1\right)\sigma_a(\lambda_m). \tag{5.145}$$

As a result of the McCumber relation in Eq. (2.32) the absorption cross section decreases exponentially with respect to the emission cross section at the long wavelength edge of the emission spectrum. Therefore, Eq. (5.145) can be always fulfilled for a given N_2 by a long-enough wavelength of the parasitic mode.

In the case of a non-perfect reflection, the condition for the onset of parasitic lasing, Eq. (5.141), results in a minimum reflection coefficient

$$R_k(\theta_a) = R_{HR}^k(\theta_a)R_{HT}^k(\theta_a)R_C(\theta_a), \tag{5.146}$$

which is given by

$$\ln R_k(\theta_a) \geq \frac{N_{tot}}{\sin\theta_a} D\left(\sigma_a(\lambda_m) - \frac{d}{D}\frac{N_2}{N_{tot}}\big(\sigma_e(\lambda_m) + \sigma_a(\lambda_m)\big)\right). \tag{5.147}$$

In the case of a perfect reflection on the HR and HT sides and $R_C(\theta_a) < 1$, we obtain a maximum gain for $\theta_a = \theta_c$. Then, the minimum reflection of the cylindrical surface is obtained as

$$\ln R_C(\theta_c) \geq N_{tot} n D\left(\sigma_a(\lambda_m) - \frac{d}{D}\frac{N_2}{N_{tot}}\big(\sigma_e(\lambda_m) + \sigma_a(\lambda_m)\big)\right). \tag{5.148}$$

It can be shown that the minimum reflection $R_C(\theta_a)$ in this case can be very small, resulting in the need for a strong control of this value in order to suppress the transverse modes. In the other important case when a non-perfect reflection $R_{HR}(\theta_a) < 1$

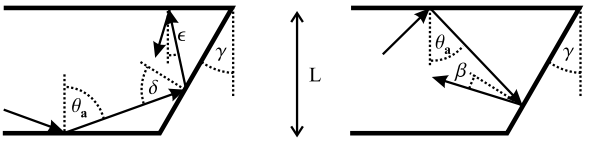

Fig. 5.55 Suppression of transverse and radial modes by a non-cylindrical disk surface

is assumed at the HR side, whilst all other sides are perfectly reflecting, we obtain a maximum gain for $\theta_a = 90° - \theta_c$. This modes shows the lowest number of reflections on the HR side. The minimum reflectivity then results in

$$\ln R_{HR}\left(90° - \theta_c\right) \geq 2nLN_{tot}\left(\sigma_a(\lambda_m) - \frac{d}{D}\frac{N_2}{N_{tot}}\left(\sigma_e(\lambda_m) + \sigma_a(\lambda_m)\right)\right). \quad (5.149)$$

In CW Yb^{3+}:YAG disk lasers this value can be as high as $R_{HR}(\theta_a) \sim 0.99$ without causing transverse modes to oscillate, whilst in Q-switched systems with a higher inversion density, the reflectivity of the HR mirror in the angular range discussed here needs to be low enough, e.g. $R_{HR}(\theta_a) < 0.8$ to suppress the transverse modes. A low HR reflectivity, however, results in a larger amount of fluorescence leaking through the HR mirror. This fluorescence gets absorbed by the heat sink and thus increases the cooling power necessary in order to maintain the disk temperature. As can also be seen in Eq. (5.149), a short crystal length L is beneficial to increase the oscillation threshold of the transverse modes. However, this has to be compensated for by a larger number of pump passes.

The radial modes do not show any total-internal reflection and oscillate through the disk center on the Fresnel reflection provided by the cylindrical disk surface, i.e. at $\theta_a = 90°$. They usually do not occur in cw lasers as a result of the low inversion density in cwW operation and the corresponding low gain. However, radial modes can occur in Q-switched disk lasers which show a much higher inversion density. The threshold for the radial modes can thus be expressed by

$$\ln R_C\left(90°\right) \geq N_{tot}D\left(\sigma_a(\lambda_m) - \frac{d}{D}\frac{N_2}{N_{tot}}\left(\sigma_e(\lambda_m) + \sigma_a(\lambda_m)\right)\right). \quad (5.150)$$

To suppress the transverse and radial modes, the outer disk surface can be shaped in a conical form shown in Fig. 5.55. Starting with an incident angle on to the bottom surface of θ_a the mode will be reflected from the outer surface and its incidence angle on the top surface will be

$$\epsilon = \mid \theta_a - 2\gamma \mid . \quad (5.151)$$

The mode is thus non-total-internal reflecting for

$$\frac{90° - \theta_c}{2} < \gamma < \theta_c, \quad (5.152)$$

which can only be fulfilled for $n < 2$, e.g. for YAG, where $28.4° < \gamma < 33.3°$. A mode reflecting totally on the upper surface needs a cone angle γ of

$$90° - 2\theta_c < \gamma < \theta_c \quad (5.153)$$

to be non-total-internal reflecting on the bottom surface, resulting in an incident angle of

$$\beta = \mid 90^\circ - \gamma - \theta_a \mid . \tag{5.154}$$

For $n < 2$, this relation is also fulfilled when Eq. (5.152) is fulfilled. Thus, for YAG, a cone angle in the range $28.4^\circ < \gamma < 33.3^\circ$ has to be chosen for transverse and radial mode suppression.

References

1. F.K. Kneubühl, M.W. Sigrist, *Laser* (Teubner, Stuttgart, 1999)
2. M. Eichhorn, S.D. Jackson, Appl. Phys. B **90**, 35 (2008)
3. W. Koechner, *Solid-State Laser Engineering* (Springer, Berlin, 1999)
4. M. Monerie, Y. Durteste, P. Lamouler, Electron. Lett. **21**, 723 (1985)
5. S.A. Payne, L.L. Chase, L.K. Smith, W.L. Kway, W.F. Krupke, IEEE J. Quantum Electron. **28**, 2619 (1992)
6. A.A. Kaminskii, *Laser Crystals*. Springer Series in Optical Science, vol. 14 (Springer, Berlin, 1990)
7. J.B. Gruber, M.E. Hills, R.M. Macfarlane, C.A. Morrison, G.A. Turner, G.J. Quarles, G.J. Kintz, L. Esterowitz, Phys. Rev. B **40**, 9464 (1989)
8. C.A. Morrison, R.P. Leavitt, Spectroscopic properties of triply ionized lanthanides in transparent host crystals, in *Handbook on the Chemistry and Physics of Rare Earths*, ed. by K.A. Gschneider Jr. (North-Holland Publishing Co., Amsterdam, 1982)
9. B.M. Walsh, N.P. Barnes, B. Di Bartolo, J. Appl. Phys. **83**, 2772 (1998)
10. S. Hufner, *Optical Spectra of Transparent Rare Earth Compounds* (Academic Press, New York, 1978)
11. B. Henderson, G.F. Imbusch, *Optical Spectroscopy of Inorganic Solids* (Clarendon Press, Oxford, 1989)
12. A. Richter, Ph.D. thesis, University of Hamburg, Germany, 2008
13. M. Alshourbagy, Ph.D. thesis, University of Pisa, Italy, 2005
14. K.M. Dinndorf, Ph.D. thesis, Massachusetts Institute of Technology, USA, 1993
15. T. Förster, Ann. Phys. **437**, 55 (1948)
16. T. Förster, Z. Naturforsch. A **4a**, 321 (1949)
17. D.L. Dexter, J. Chem. Phys. **21**, 836 (1953)
18. C.Z. Hadad, S.O. Vasquez, Phys. Rev. B **60**, 8586 (1999)
19. P.M. Levy, Phys. Rev. **177**, 509 (1969)
20. F.R.G. de Silva, O.L. Malta, J. Alloys Compd. **250**, 427 (1997)
21. V.S. Mironov, J. Phys. Condens. Matter **8**, 10551 (1996)
22. M. Yokota, O. Tanimoto, J. Phys. Soc. Jpn. **22**, 779 (1967)
23. A.I. Burshtein, Sov. Phys. JETP **35**, 882 (1972)
24. T. Holstein, S.K. Lyo, R. Orbach, in *Topics in Applied Physics*, vol. 49, ed. by W.M. Yen, P.M. Selzer (Springer, New York, 1981). Chap. 2
25. R. Orbach, in *Optical Properties of Ions in Crystals*, ed. by H.M. Crosswhite, H.W. Moos (Interscience, New York, 1967), p. 445
26. S. Xia, P.A. Tanner, Phys. Rev. B **66**, 214305 (2002)
27. S.D. Jackson, Opt. Commun. **230**, 197 (2004)
28. A. Hoffstaedt, Festkörper-Laser-Institut Berlin, Germany, 1991
29. M. Rattunde, Ph.D. thesis, University of Freiburg i. Br, Germany, 2003
30. D. Gloge, Weakly guiding fibers. Appl. Opt. **10**, 2252 (1971)
31. B.M. Walsh, N.P. Barnes, Appl. Phys. B **78**, 325 (2004)

32. B.M. Walsh, Private communication
33. M. Eichhorn, A. Hirth, in *Conference on Lasers and Electro-Optics CLEO 2008*, San Jose, USA. Paper CTuII3
34. M. Eichhorn, Opt. Lett. **32**, 1056 (2007)
35. M. Eichhorn, in *Conference on Lasers and Electro-Optics CLEO 2007*, Baltimore, USA. Paper CTuN7
36. M. Eichhorn, S.D. Jackson, Opt. Lett. **32**, 2780 (2007)
37. M. Eichhorn, S.D. Jackson, in *Conference on Lasers and Electro-Optics CLEO 2008*, San Jose, USA. Paper CFD7
38. M. Eichhorn, in *OPTRO 2005 Symposium*, Ministère de la Recherche, Paris, France, 9–12 May 2005
39. M. Eichhorn, in *Journées Scientifiques de l'ONERA: Lasers et amplificateurs à fibre optique de puissance: fondements et applications*, ONERA, Châtillon, France, 27–28 June 2005
40. M. Eichhorn, Opt. Lett. **30**, 456 (2005)
41. M. Eichhorn, Opt. Lett. **30**, 3329 (2005)
42. M. Eichhorn, Virtual J. Ultrafast Sci. **5**(1) (2006)
43. G.P. Agrawal, *Nonlinear Fiber Optics* (Academic Press, San Diego, 2001)
44. D. Cotter, J. Opt. Commun. **4**, 10 (1983)
45. L.G. Hwa, J. Schroeder, X.S. Zhao, J. Opt. Soc. Am. B **6**, 833 (1989)
46. Y. Durteste, M. Monerie, P. Lamouler, Electron. Lett. **21**, 723 (1985)
47. K. Contag, Dissertation, University of Stuttgart, Germany, 2002
48. D. Marcuse, Bell Syst. Tech. J. **55**, 703 (1977)
49. S.P. Timoshenko, J.N. Goodier, *Theory of Elasticity*, 3rd ed. (McGraw-Hill, New York, 1970)